Nanoscale Advances

ROYAL SOCIETY OF CHEMISTRY

PAPER

View Article Online
View Journal | View Issue

Cite this: *Nanoscale Adv.*, 2025, **7**, 6575

Zirconium ferrite nanoparticles as smart materials for energy and environmental applications: fractional-order supercapacitors, reservoirs of F^- ions, and efficient electrocatalysts for water splitting

Amit Sahoo, [a] Achyuta N. Acharya, *[a] Priyambada Jena,[a] M. Moonis,[a] J. P. Biswal,[a] S. Swain[b] and M. C. Tripathy[b]

A novel electrocatalyst, zirconium ferrite nanoparticles (NPs) ($ZrFe_2O_5$ NPs), was synthesized through coprecipitation and calcination processes at 300 °C and 500 °C using iron rust. The $ZrFe_2O_5$ NPs were used as catalysts for the hydrogen evolution reaction. Furthermore, these NPs in an alkaline medium exhibited superior properties of a fractional order supercapacitor, based on which a prototype device was fabricated to demonstrate its energy storage applications. The capacitance and phase graphs of the fractional-order supercapacitor exhibit a peak value of 1.5 F $s^{-1-\alpha}$ in the mid-frequency range, followed by a decrease at increased frequencies. Furthermore, these NPs were found to be the most effective agents for removing fluoride ions. In a modified one-pot synthetic approach, the hydrogel (Hy) was synthesized using PVA and glycerine in an aqueous medium at 100 °C. The composite Hy membranes were prepared by mixing Hy with these NPs, which were applied to remove fluoride ions efficiently within the pH range of 1–10 from the aqueous medium through adsorption, yielding defluorinated water. The adsorption process of fluoride ions was correlated with the Freundlich and Langmuir isotherms, with pseudo-second-order kinetics as the preferred approach. The zirconium ferrite NPs and the composite Hy membranes were characterized through various characterization techniques, *i.e.*, XRD, XPS, FTIR, solid UV-visible spectroscopy, STA, FESEM, HRTEM, and BET surface area analysis.

Received 12th June 2025
Accepted 10th August 2025

DOI: 10.1039/d5na00578g

rsc.li/nanoscale-advances

1. Introduction

Iron corrosion is primarily caused by exposure to oxygen, moisture, water, and air, resulting in the formation of iron rust, which is considered a waste material.[1] Iron oxides from corroding pipes can result in particulate matter pollution, negatively impact plant growth and soil chemistry, and contaminate drinking water.[2,3] Despite its numerous applications, including pigments, catalysts, and environmental remediation, its disadvantages significantly limit its potential. The material has several deficiencies, including a fragile structure, reduced reactivity relative to customized oxides or pure iron, and the potential for heavy metal contamination and uncontrolled dispersion, which heightens environmental concerns.[4] Moreover, its irregular particle size and heterogeneous composition sometimes render it inefficient for advanced applications such as catalysis and batteries.[5] The environmental implications, performance enhancement, and safe utilization of iron oxide powders derived from rust in high-value applications remain inadequately explored, notwithstanding the growing interest in recycling these materials.[2]

Human survival relies on water safety and purity, with concerns about fluoride concentration in drinking water.[6] Excessive fluoride in industrialized and developing nations causes dental fluorosis. Artificial fluoridation sources, sourced from phosphate industry waste, are not of pharmaceutical quality.[7,8] Over time, various approaches have been investigated to remove excess fluoride from water, including adsorbents, filtration methods such as reverse osmosis and nanofiltration, and electrochemical methods. The adsorption method is a practical and economical technique for removing heavy metals and fluoride, especially with polymers like chitosan, PVA, and their composites.[6,9–14] Nanocellulose-based materials with surface alterations exhibit higher adsorption capabilities for heavy metals, fluoride, and dyes,[15,16] while advanced modifications such as crosslinking and grafting have improved adsorption capacity and durability.[6,9–14] Bi- and multi-metal

[a]*School of Basic Sciences & Humanities (Chemistry), Odisha University of Technology and Research, Bhubaneswar-751029, Odisha, India. E-mail: aacharya@outr.ac.in; amitsahoochemistry@gmail.com*

[b]*School of Electronic Science, Odisha University of Technology and Research, Bhubaneswar, India*

ferrites and nanocomposites have demonstrated favorable fluoride adsorption from aqueous solutions.[10,17]

Hydrogen, a clean and sustainable energy source, can be produced through water electrolysis.[18] Water is oxygenated to O_2 at the anode, releasing protons and electrons that are used at the cathode to produce H_2.[19] However, the efficiency of the anodic oxygen evolution reaction (OER) is limited by its slow kinetics, which produces a significant overpotential. Non-noble metal OER electrocatalysts, such as Ni-based (oxy)hydroxides, make alkaline water electrolysis (AWE) an inexpensive option; however, it still has an overpotential of over 200 mV.[20] Hydrogen gas is a sustainable energy source that can substitute for fossil fuels in applications such as fuel cells, energy storage, chemical manufacturing, and petroleum refining. The primary method of hydrogen production is natural gas cracking, which is not environmentally sustainable.[21–24] Renewable energy sources such as wind, tidal, or solar can provide electrochemical water splitting (EWS) for hydrogen gas production. Developing modern agents as catalysts for increased EWS reactions could mitigate the energy challenges.[25]

Bi-metal oxides, particularly ferrites,[26] are used as electrocatalysts for water splitting, as they are affordable, environmentally friendly, and highly effective.[8–11,17,18,27,28] Debnath *et al.*[29] investigated cobalt ferrite ($CoFe_2O_4$) nanoparticles with controlled oxygen vacancies, synthesized *via* coprecipitation and inert calcination, which display bifunctional electrocatalytic performance for the hydrogen evolution reaction (HER) and oxygen evolution reaction (OER), necessitating minimal overpotentials and showcasing exceptional durability in water electrolysis. Fatima *et al.*[30] reported the development of a composite electrode comprising cobalt ferrite nanoparticles attached to carbon nanotube fibers, which enabled enhanced electrocatalytic efficacy for water splitting in alkaline environments, with notable improvements in conductivity and stability. Li *et al.*[31] studied the synthesis of $MnFe_2O_4$ nanofibers using electrospinning, resulting in a three-dimensional porous structure with enhanced electrocatalytic performance for the oxygen evolution reaction and hydrogen peroxide reduction.

Hybrid supercapacitors (HSCs)[32,33] prevail in the energy storage sector, although generation-I electrochemical energy conversion and storage systems (EECSs) represent the most environmentally sustainable technology. Strategic methodologies and electrode compositions drive the advancement of generation-II electrodes and hybrid energy devices.[34] Freeborn *et al.*[35] conducted a comprehensive review of existing fractional-order models employed in hybrid and renewable energy systems, encompassing supercapacitors, batteries, and fuel cells. These models optimally fit experimentally observed impedance values and transient responses, utilizing one or more constant phase elements (CPEs), also known as fractional-order capacitors.

A $ZrCoFe_2O_4$/NrGO nanocomposite, designed as an electrode material for supercapacitors, was investigated by Kenari *et al.*[36] and exhibited a specific capacitance of 307 F g^{-1} at 1 A g^{-1}. After

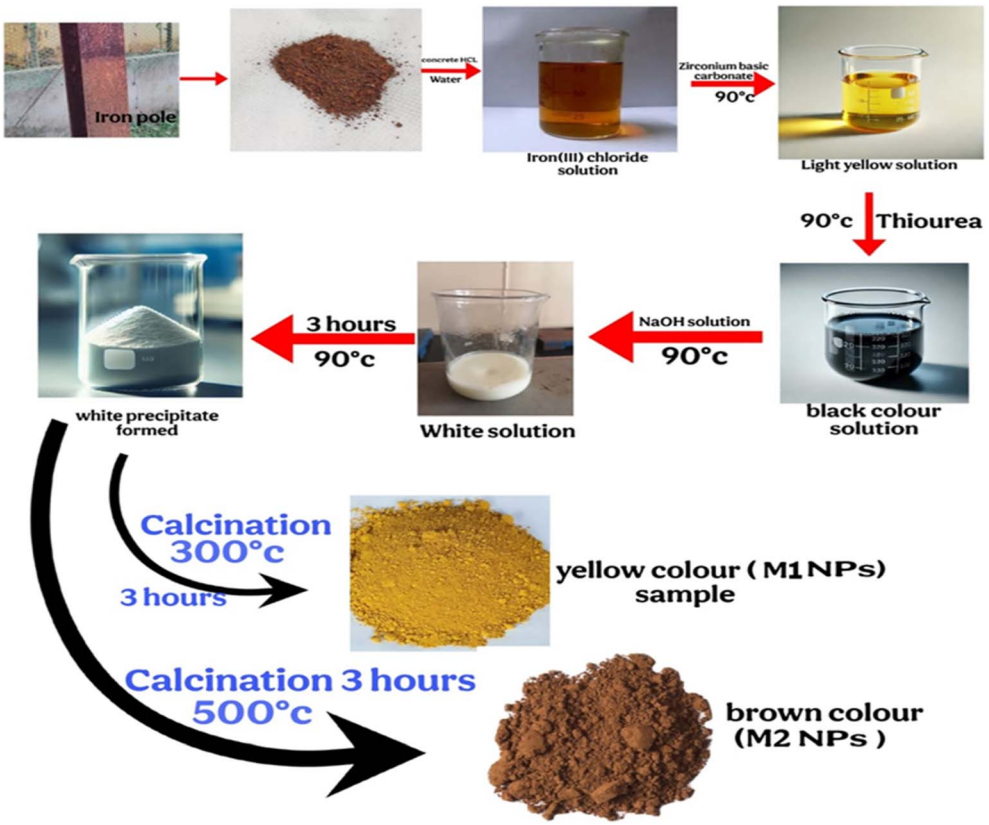

Scheme 1 Schematic diagram of the synthesis of M2 and M1 NPs.

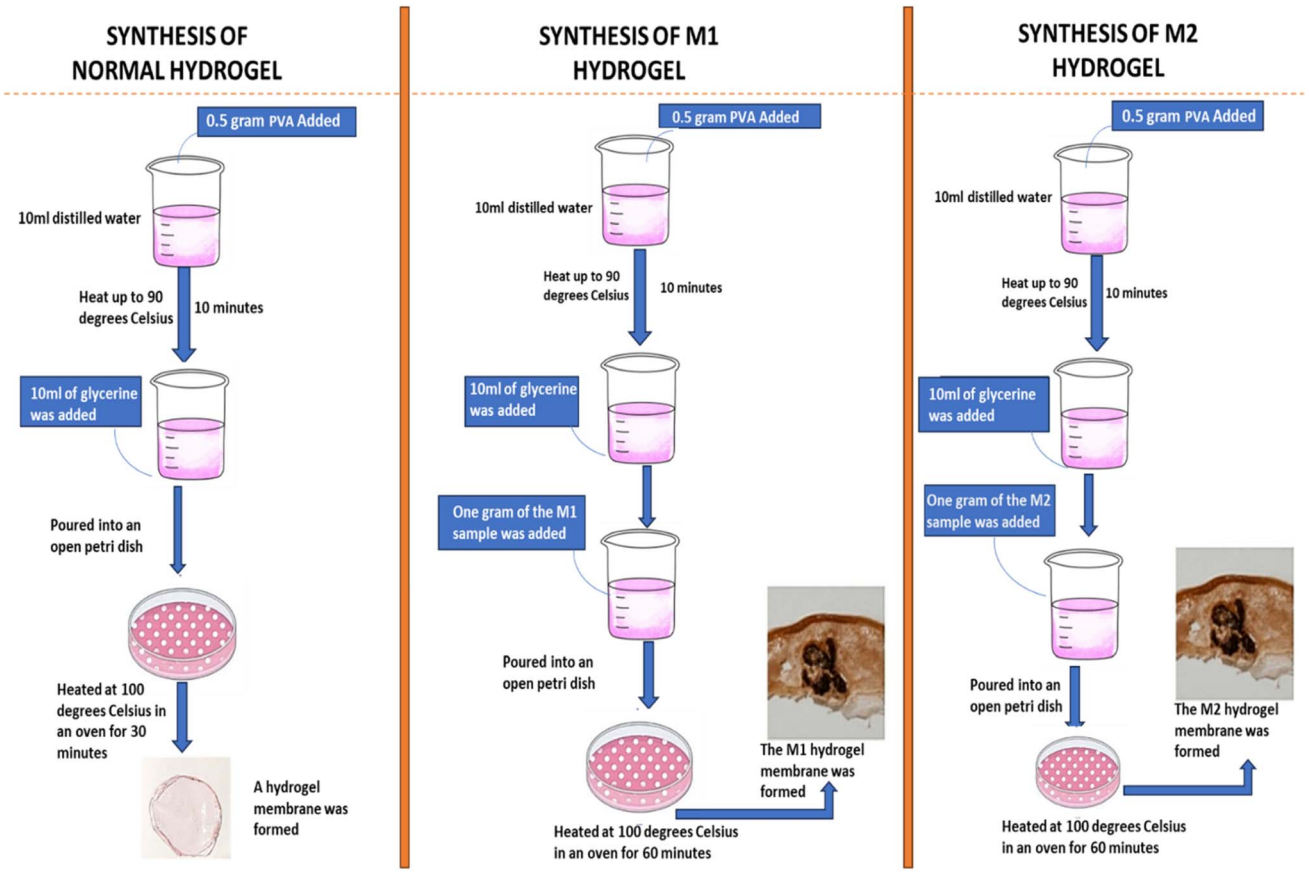

Scheme 2 Schematic synthesis diagram of Hy, Hy(M2) and Hy(M1).

5000 cycles, its stability remained at approximately 97%, indicating strong electrochemical stability. Allagui *et al.*[37] studied the charging voltage profile that affects the discharge voltage pattern of a supercapacitor, which displays fractional-order behavior. Due to its history-dependent dynamic behavior, the charging waveform pattern can yield unique information. The information storage mechanism is explained using an analytical model based on fractional calculus, which may result in new information retrieval and storage techniques.

It is the first of its kind that a waste material, *i.e.*, iron rust, in which iron exists mainly Fe_2O_3,[38] is used as the source of Fe^{3+} for the synthesis of zirconium ferrite nanoparticles (NPs). The hydrogel (Hy) is synthesized using a modified method, which is a novel, cost-effective, and one-pot synthesis method that utilizes polyvinyl alcohol (PVA) and glycerine. The composite of zirconium ferrite NPs with Hy is synthesized, and its membrane is used for the efficient adsorption of fluoride ions. These NPs exhibit inimitable properties, such as energy storage

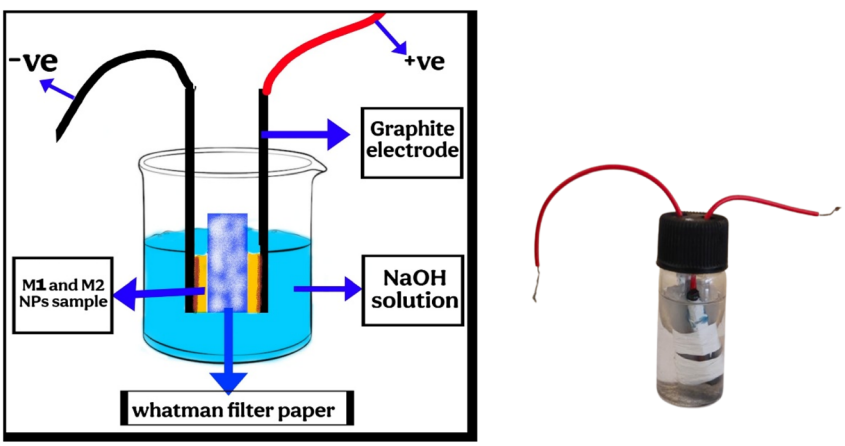

Scheme 3 Schematic diagram of the M2/M1 NP-based device for electronic applications.

applications, producing defluorinating water with efficient removal of fluoride ions from aqueous solutions, and promoting sustainable energy production by producing green hydrogen gas through EWS. These NPs can also be utilized as fractional-order supercapacitors.

2. Experimental section

2.1. Methods

2.1.1. Materials and reagents. Iron rust powders (collected from rusted iron electric poles), concentrated hydrochloric acid (Loba), sodium hydroxide (Analar grade, Loba), and thiourea (Extra Pure, Merck) were used as chemical reagents for the synthesis of zirconium ferrite NPs. Polyvinyl alcohol (Extra Pure, PVA, Loba) and glycerine (Extra Pure Merck) were used as chemical reagents for synthesizing Hy membranes. Sodium fluoride (Analar Grade, Loba) was used to study fluoride ion adsorption. Highly purified graphite electrode bars and sodium hydroxide (Analar grade, Loba) were used to study the electrochemical and electronic applications. Millipore-distilled water was used as the solvent for all experiments.

2.1.2. Synthesis of zirconium ferrite NPs. Primarily, iron exists in its +3 oxidation state (Fe^{3+}) in rusted iron.[38–40] Iron rust (2 g) was taken in a beaker and dissolved in 50 mL of concentrated HCl for 1 hour, and then 50 mL of distilled water was added and the mixture was stored for ~24 hours at room temperature. The solution was filtered, and the filtrate contained only Fe^{3+}, as established by a confirmatory test for Fe^{3+} using NaSCN[38–42] as no detectable Fe^{2+} was found. The filtrate

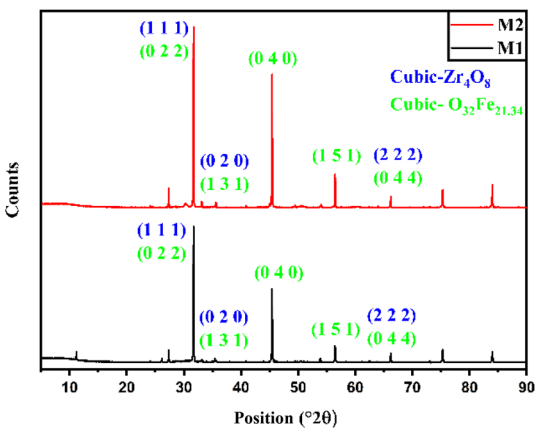

Fig. 1 The XRD pattern of the M2 and M1 NPs.

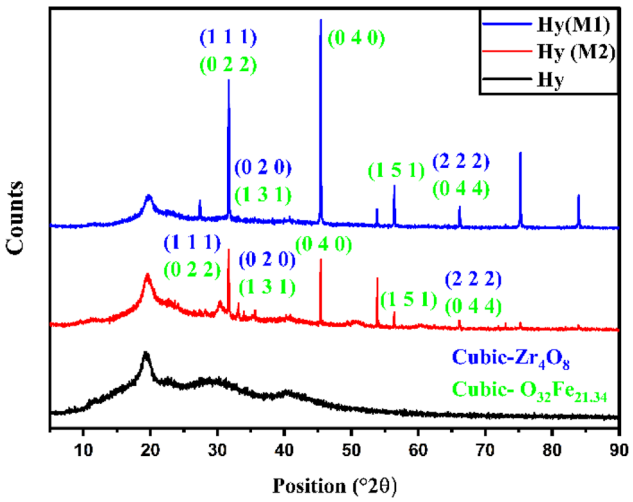

Fig. 2 The XRD pattern of the Hy, Hy(M2), and Hy(M1) samples.

Table 1 The XRD peaks analysis data of the M2 and M1 NPs

Sample name	No.	2 Theta [°]	FWHM [°]	*d*-Spacing [Å]	Miller indices (*h k l*) (cubic-Zr_4O_8)	Miller indices (*h k l*) (cubic-$O_{32}Fe_{21.34}$)	Intensity (%)	Crystalline grain size (nm)
M2	1	31.69738	0.072	2.8206	(1 1 1)	(0 2 2)	100	2.00
	2	35.62557	0.072	2.51808	(0 2 0)	(1 3 1)	2.72	2.02
	3	45.44542	0.096	1.99419	(– – –)	(0 4 0)	73.79	1.56
	4	56.45956	0.096	1.62851	(– – –)	(1 5 1)	18.14	1.63
	5	62.42435	0.096	1.48646	(2 2 2)	(0 4 4)	0.63	1.68
M1	1	31.70494	0.096	2.81994	(1 1 1)	(0 2 2)	100	1.50
	2	35.43682	0.096	2.53105	(0 2 0)	(1 3 1)	2.65	1.51
	3	45.44399	0.096	1.99425	(– – –)	(0 4 0)	54.12	1.56
	4	56.46284	0.096	1.62842	(– – –)	(1 5 1)	11.87	1.63
	5	62.41375	0.144	1.48669	(2 2 2)	(0 4 4)	0.31	1.12

Table 2 The lattice constants of the M2 and M1 NPs

Sample name	Crystal system	Lattice constant	Standard values (Å)	Calculated value (Å)
M2	Cubic-Zr_4O_8	$a = b = c$	5.0900	5.0361
	Cubic-$O_{32}Fe_{21.34}$	$a = b = c$	8.4050	8.4619
M1	Cubic-Zr_4O_8	$a = b = c$	5.0900	5.0621
	Cubic-$O_{32}Fe_{21.34}$	$a = b = c$	8.4050	8.4615

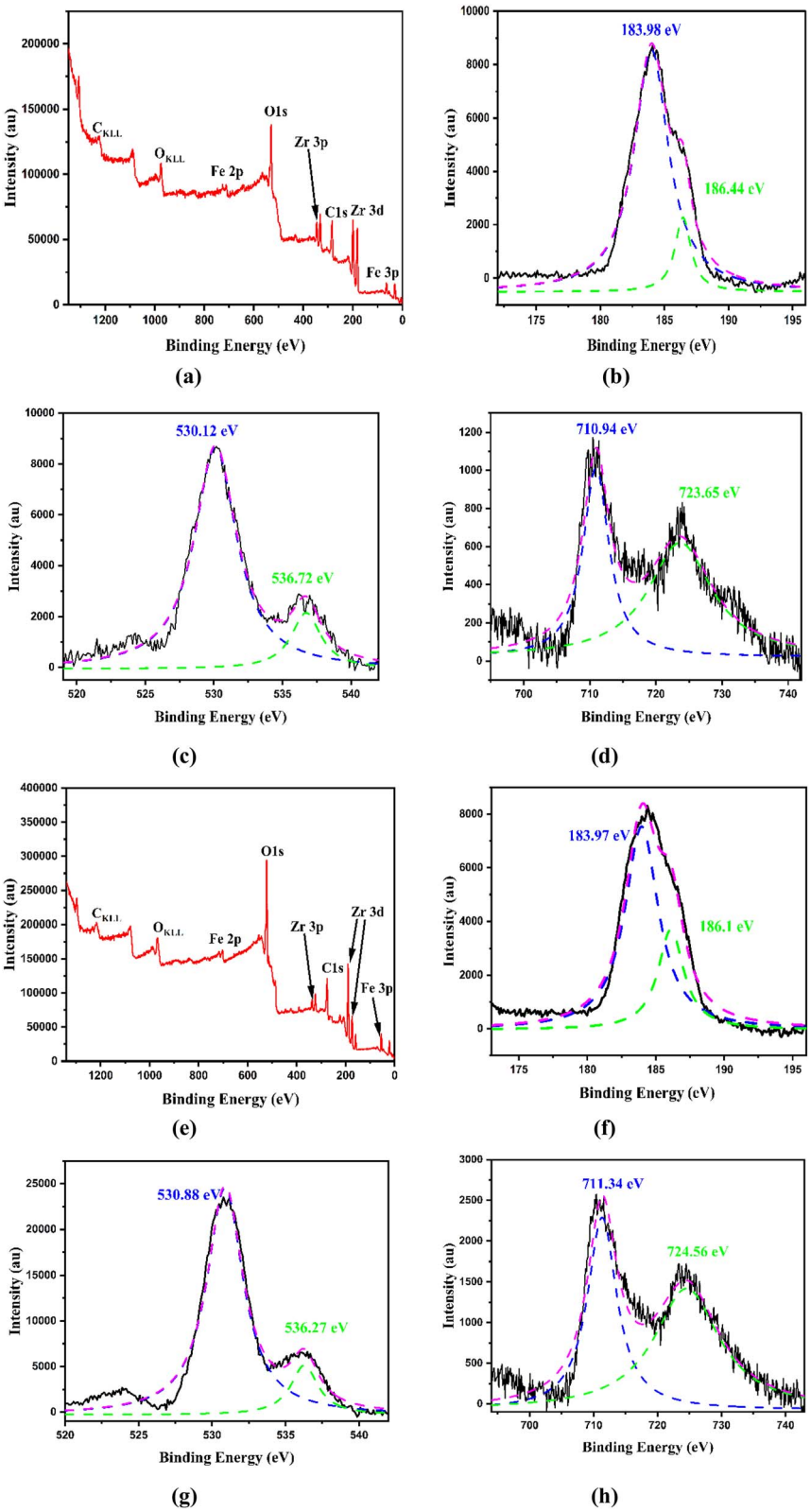

Fig. 3 The XPS survey patterns of the (a) M2 and (e) M1 NP samples. The high-resolution XPS patterns: for Zr 3d peaks of the M2 (b) and M1 (f) NP samples; for O1s peaks of the M2 (c) and M1 (g) NP samples; for Fe 2p peaks of the M2 (d) and M1 (h) NP samples.

$FeCl_3$ solution was quantitatively analyzed using $KMnO_4$ (0.01 N) in the presence of H_2SO_4 (6 N).[43] Then, 100 mL of the 0.05 N $FeCl_3$ solution (a light brown solution) was taken in a beaker, and 1.53 g of $ZrCO_3$ was added at 90 °C with continuous stirring at 1000 rpm. The solution color turned light yellow after $ZrCO_3$ was fully dissolved in the acidified $FeCl_3$ solution. Then, the

color of the solution turned black on the addition of 5 g of thiourea. To this mixture, NaOH was gradually added to maintain the pH at ~10 with continuous stirring at 1000 rpm over 3 hours until a white precipitate was formed at 90 °C which was then calcined in a furnace at two different temperatures: 300 °C (yielding sample M1, yellow color) and 500 °C (yielding sample M2, brown color). The M2 and M1 samples were converted into fine particles using a mortar and pestle, rinsed with distilled water (for removing excess reagents), isolated from the solvent using centrifugation at 10 000 rpm for 10 minutes, and dried in an oven at 90 °C for 1 hour (Scheme 1).

2.1.3. Synthesis of Hy membranes and zirconium ferrite NP–Hy composite membranes. A modified synthetic approach was employed, in which 2.55 mM PVA with 6.84 M glycerine in a 20 mL aqueous solution was stirred at 90 °C for 10 min to form a mixture (PVA–glycerine mixture), followed by heating for 30 minutes at 100 °C to crosslink the polymer, yielding Hy.

However, the composite of zirconium ferrite NPs with Hy was synthesized in one step wherein 1 gram of M2/M1 NPs was added to the PVA–glycerine mixture (as described above) with stirring for 3–5 min to form a uniform mixture. Then, this was heated for one hour at 100 °C to synthesize Hy(M2)/Hy(M1) [Hy(M1): the composite of M1 zirconium ferrite NPs with Hy; and Hy(M2): the composite of M2 zirconium ferrite NPs with Hy].[44] In both the composites, Hy(M2) or Hy(M1), the Hy: zirconium ferrite NP ratio was 1 : 1 (w/w in grams). The membranes of Hy and both composites were prepared using a Petri dish (Scheme 2).

2.1.4. Fabrication of two electrode-based devices for electronic application. Graphite rod electrodes were used as the anode and cathode current collectors in the electrochemical cell, which was constructed using a 20 mL glass sample tube as the housing. Polyvinylidene fluoride (PVDF) polymer and the sample M2/M1 NPs were mixed at a weight ratio of 8 : 2 g to fabricate the electrode-active material, where NMP (*N*-methyl-2-pyrrolidone) was used as a binder solvent. The uniform mixture of PVDF, NMP, and M2/M1 NP was coated on the surface of the graphite rod, in which each graphite electrode's tip was covered with a specific area of 0.48 cm^2 (1.2 cm in length and 0.4 cm in width). The coated electrodes were dried in a hot oven at 90 °C to promote adhesion and remove any remaining solvent.

The electrodes were gently inserted through two holes drilled into the glass sample tube's top cover to include them in the configuration. Then, 15 mL of 3 M NaOH solution was added to the completed cell to submerge the active material and guarantee complete electrolyte immersion. The electrochemical cell was then used to test the charge storage and energy retention properties of a fractional-order supercapacitor[45] (Scheme 3).

2.1.5. Characterization techniques. A Bruker D8 Advance powder X-ray diffraction (PXRD) device was used to investigate the phases of the M2, M1 NPs, Hy, Hy(M2), and Hy(M1). The XRD patterns were obtained using a monochromatic Cu Kα (λ = 1.5418 Å) radiation source, and the diffraction profiles were recorded with an angular increment of 0.029° (2θ) over a 2θ range of 5° to 90°. The crystal lattice structures were examined using X'Pert HighScore Plus software. The International Centre for Diffraction Data provided the data as a Powder Diffraction File (PDF), which agreed with the XRD data, namely the *d*-spacing of the M2 and M1 NP samples.

The elemental detection and oxidation states of Zr, and Fe in the M2 and M1 NP samples were determined using X-ray Photoelectron Spectroscopy (XPS) with an X-ray photoelectron spectrometer (Thermo Fisher Scientific Instruments, UK, Model-K ALPHA). A source–analyzer setup at a 45° angle was used for these investigations.

Fourier Transform Infrared Spectra (FTIR) were recorded at approximately 25 °C between 400 and 4000 cm^{-1} using a PerkinElmer Spectrum Two instrument with potassium bromide as the reference material. The bandgap energy of the M2 and M1 samples was determined by recording the UV-visible (solid) spectra using a UV-Visible spectrometer (Jasco, V-770). The band gap energy of the M2 and M1 samples was determined using the Tauc plot method.

The thermal stability of the M2 and M1 samples, as assessed using a Simultaneous Thermal Analyzer (STA) (TGA: thermogravimetric analysis and DSC: Differential Scanning Calorimetry), was evaluated using a PerkinElmer STA 6000 instrument in the temperature range of 30–900 °C at a heating rate of 10 °C min^{-1}. The thermal behavior of the M2 and M1 samples was characterized by analyzing the time *versus* weight loss percentage and time *versus* heat flow graphs.

A JEOL FESEM (JSM-7610F) instrument was used to examine the surface morphology of the M2, M1 NPs, Hy, Hy(M2), and Hy(M1) samples utilizing the Field Emission Scanning Electronic Microscope (FESEM) technique. This technique involved placing the samples on carbon tape and then coating them with gold for around 60 s.

The internal morphology of the M2 and M1 NPs was examined using High-Resolution Transmission Electron Microscopy (HRTEM) using a JEOL HRTEM (JEM-2100 Plus) instrument. In this case, a 300-mesh carbon-coated copper grid (Merck, India) served as the standard/reference.

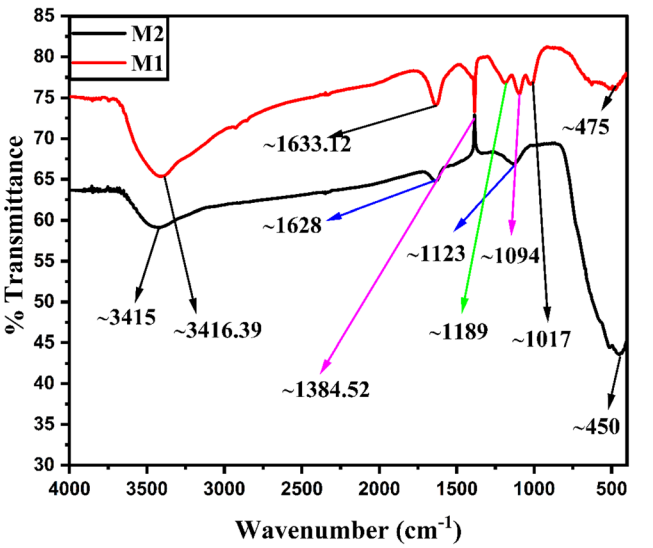

Fig. 4 The FTIR spectra of M2 and M1 NPs.

An Autosorb iQ Station 1 was used in the Brunauer–Emmett–Teller (BET) surface area analysis, which uses gas adsorption to determine an analyte's specific surface area. Using this technique, a solid sample is either suspended in a known volume of gas or passed over an inert gas, such as nitrogen.

An Epsilon (E21170 model) three-electrode system workstation was used for the electrochemical analysis of the M2 and M1 NP samples in the presence of a NaOH solution as the electrolyte. For electrochemical analysis, the electrodes are made using a graphite rod, PVDF, NMP, and NP material M2 and M1. The "Fabrication of two electrode-based devices for electronic application" section discusses the electrode fabrication process. The Ag/AgCl electrode (Basi, MF-2052) served as the reference electrode, and the platinum electrode (Basi, MW-1032) acted as the counter electrode for the analysis.[46]

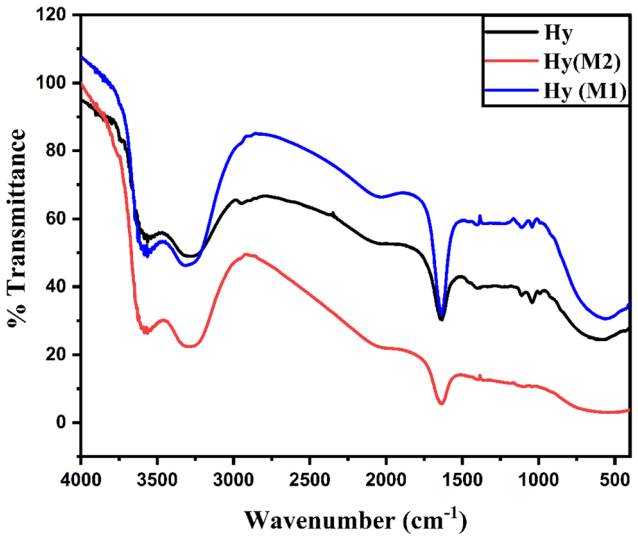

Fig. 5 The FTIR spectra of the Hy, Hy(M2), and Hy(M1) samples.

The concentration of F^- ions (ppm) in the solution at room temperature was measured using a Thermo Scientific Orion Versastar Pro advanced electrochemistry meter with an Orion 9609BNWP ionplus sure-flow fluoride electrode.[47]

3. Results and discussion

3.1. Phase and crystallographic analysis

The *d*-spacing values of the NPs (calculated from 2θ and FWHM of the peaks from XRD patterns; Fig. 1) and the positions of these peaks were matched with the International Centre for Diffraction data PDFs (Powder Diffraction File) No. 96-152-1754 (Zr_4O_8, Cubic) and 96-152-8612 ($O_{32}Fe_{21.34}$, Cubic) for both M1, and M2 NPs.[48] The values of Miller indices ($h\ k\ l$) (obtained from PDF files) and the crystalline grain sizes (calculated using *d*-spacing) of the M2 and M1 NPs are given in Table 1. The M2 and M1 NPs have average crystalline grain sizes of ($\approx$) 1.77 and 1.46 nm, respectively. The computed values of the lattice constants, listed in Table 2, agree well with the PDF data for both M2 and M1 NPs.

The XRD patterns of the Hy, Hy(M1), and Hy(M2) membranes in the 2θ range of 5–90° are presented in Fig. 2. Due to the copolymer Hy networks, the pure Hy XRD pattern exhibits a prominent broad peak at ~20°, indicating the formation of three humps in the amorphous region. The M1 and M2 NP XRD peaks were observed with the Hy peak in the case of their composites, Hy(M1) and Hy(M2).

The XRD analysis confirmed the zirconium ferrite compositions for M2 and M1 NPs. In the M2 NP XRD pattern, there was another small peak (very low intensity) obtained at around 30° for the ZrO_2 detaching from the zirconium ferrite NP crystal lattice due to the high-temperature calcination. Kaur *et al.*[49] studied zirconium ferrite nanoparticles synthesized by the hydrothermal synthesis method and calcined at temperatures between 300 °C and 700 °C. The crystal phases typically range

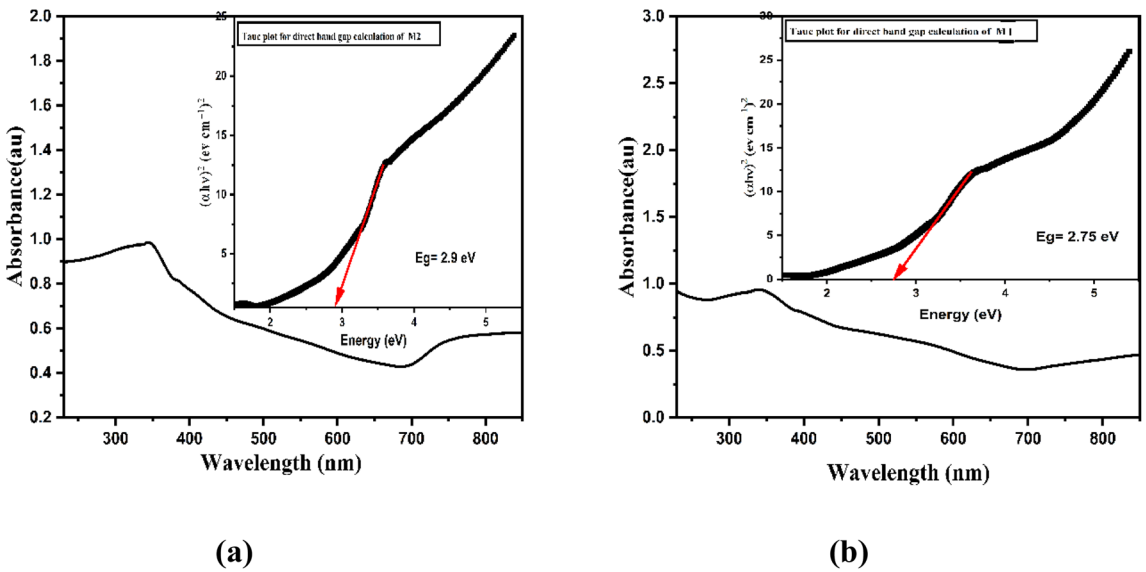

Fig. 6 The band gap energy study of the (a) M2 NPs and (b) M1 NPs.

from 1.1 to 2.0 nm, and this range increases with an increase in temperature (Table 1). Strong peaks, corresponding to spinel ferrite phases, hematite α-Fe_2O_3, and tetragonal ZrO_2 phases, were observed at higher temperatures after the initially amorphous materials were calcined. The presence of M2 and M1 NP XRD peaks with the Hy peak in the case of Hy(M2) and Hy(M1) confirmed the binding of the NPs in the Hy sample.[50]

3.2. XPS analysis

The XPS survey spectra of the M2 (Fig. 3a) and M1 NP (Fig. 3e) samples confirm the presence of 100% pure zirconium, iron, and oxygen elementary species. The high-resolution XPS patterns for Zr 3d, O1s, and Fe 2p peaks of the M2 and M1 NP samples (SI in Table 1) confirm their compositions as zirconium ferrite nanoparticles.[51] Zirconium exists in its +4 oxidation state, Zr^{4+}, which conforms with the binding energy estimates of Zr $3d_{5/2}$ and Zr $3d_{3/2}$ (SI in Table 1) for the M2 (Fig. 3b) and M1 NPs (Fig. 3f) samples.[52–54] Symmetric broadening at binding energy was revealed by analyzing high-resolution XPS O1s spectra in M2 (Fig. 3c) and M1 (Fig. 3g) NP samples, revealing a covalent link between the oxygen atom and two metal cations like Fe–O–Fe/Fe–O–Zr/Zr–O–Zr.[53] The binding energy estimates of Fe $2p_{3/2}$ and Fe $2p_{1/2}$ (SI in Table 1) for the M2 (Fig. 3d) and M1 NPs (Fig. 3h) samples are consistent with the +3 oxidation

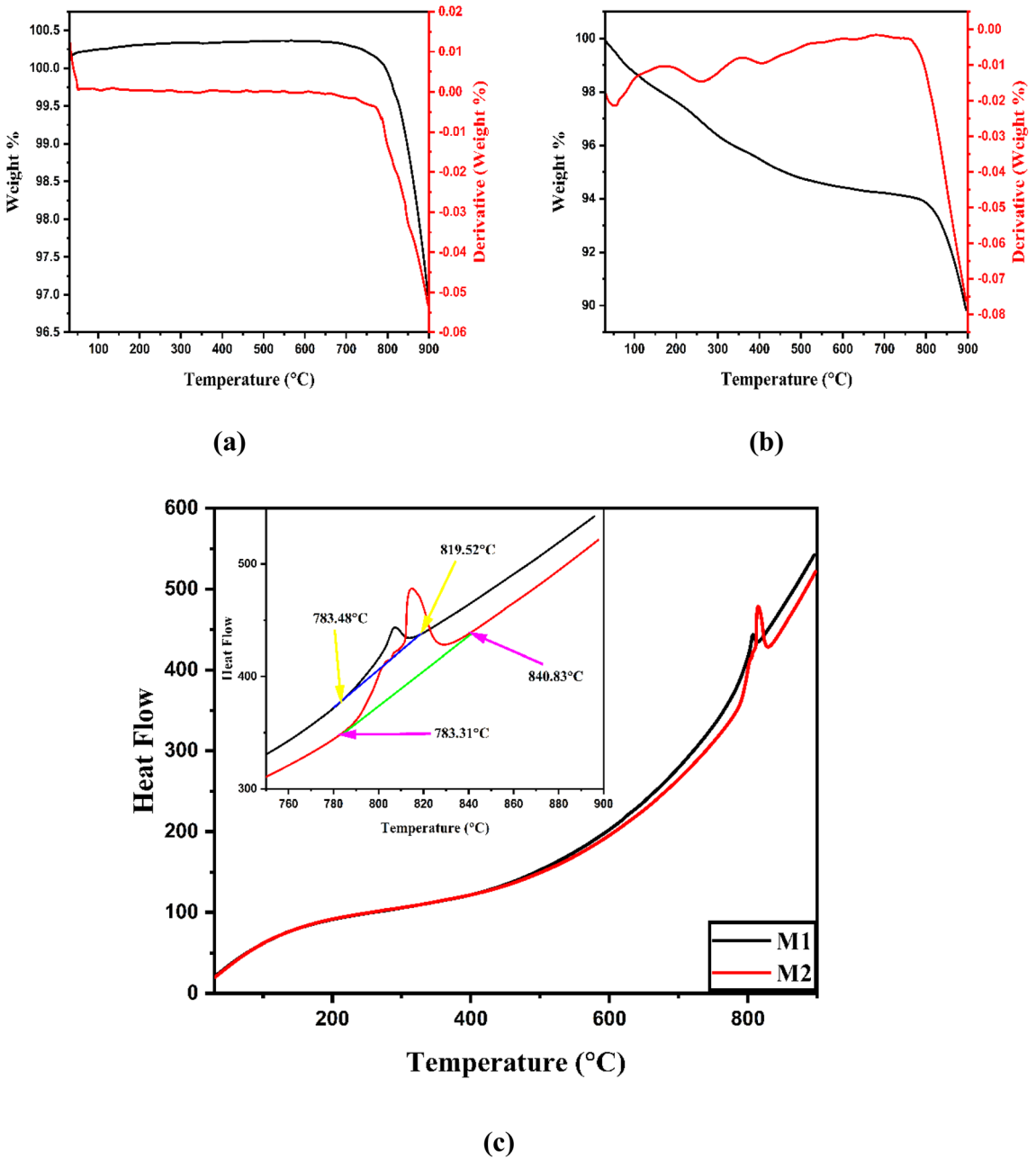

Fig. 7 TGA and DTG curves: (a) M2 NPs and (b) M1 NPs; (c) DSC curve of the M2 and M1 NPs.

state of Fe.[52–54] The presence of Fe^{2+} was not observed in the XPS spectra. Hence, the XPS and XRD data analysis of the M2 and M1 NP samples confirmed the presence of 100% pure zirconium ferrite NPs as $ZrFe_2O_5$ NPs.[45,52–54]

3.3. FTIR analysis

The bond characteristics of M2, M1 NPs (Fig. 4), Hy, Hy(M2), and Hy(M1) (Fig. 5) were studied using FTIR analysis in the 400–4000 cm^{-1} range at ~25 °C. For M2 and M1 NPs, the –OH stretching and bending vibrations of adsorbed water are indicated by the peaks at ~3415 and ~1628 cm^{-1}.[55] The O–H bonding is responsible for the band observed at ~1384 cm^{-1}.[56] The peaks in the 1000–1200 cm^{-1} range may correspond to the stretching vibration of the C–O bond of environmental CO_2 bound on the surface of the NPs.[57] While the 400–700 cm^{-1} band corresponds to Zr–O vibration with Fe–O in the cubic structure and nanocrystals, the strong band implies indifferent energy bonding states.[55,58]

There are two broad peaks in the 3000–3600 cm^{-1} range due to the O–H stretching vibration of the hydroxyl group of glycerine and PVA. There is a diminished peak at around 2942 cm^{-1} for the aliphatic C–H stretching vibration of the Hy membrane due to the crosslinking of PVA and glycerine.[59–62] A carbon–hydrogen bond located on a hydrocarbon chain in the polymer network of Hy is known as an "aliphatic CH bond".[44] C=C bond stretching vibrations of the Hy membrane are responsible for the initial vibration peak at ~1635 cm^{-1}.[44] The ether group (–C–O–C–) stretching vibration peaks in the 1000–1200 cm^{-1} range result from the formation of ether group and are characteristic of crosslinking between PVA and glycerine in the Hy membrane.[59–62] The shift in positions and changes in intensities of the peaks of Hy in the case of Hy(M2) and Hy(M1) may correspond to the binding of the NPs in the Hy membrane.

3.4. Band gap energy analysis

The Tauc plot approach[63,64] (SI as E1) from the UV-visible spectra was adopted for the determination of the direct band gap energy of M2 NPs (Fig. 6a) and M1 NPs (Fig. 6b). The direct band gap energies of ~2.9 and 2.75 eV were obtained for M2 (calcined at 500 °C) and M1 (calcined at 300 °C) NPs, which confirmed that both NP samples are semiconductors.[65] The band gap energy analysis showed that the band gap energies increased when the calcination temperature increased, which was confirmed by the size of the crystallites obtained from the XRD analysis[49] (Table 2).

3.5. Simultaneous thermal analysis (STA: DSC + TGA)

The thermal stability of the M2 and M1 NPs was studied at temperatures ranging from 30 to 900 °C at a rate of 10 °C s^{-1}. The TGA, DSC, and DTG (derivative thermogravimetry) curves of M2 NPs demonstrated their stability up to temperatures of around 700 °C. The DTG curve (Fig. 7a) shows a peak at around 50 °C due to moisture evaporation. The TGA and DTG (Fig. 7b) curves of M1 NPs show multiple weight losses of around 4% and exothermic peaks for surface and void moisture evaporation at 30–400 °C range temperature. The DSC curve (Fig. 7c) of M2 and M1 NPs also confirmed that the exothermic reaction occurs at a temperature range of around 750–900 °C.

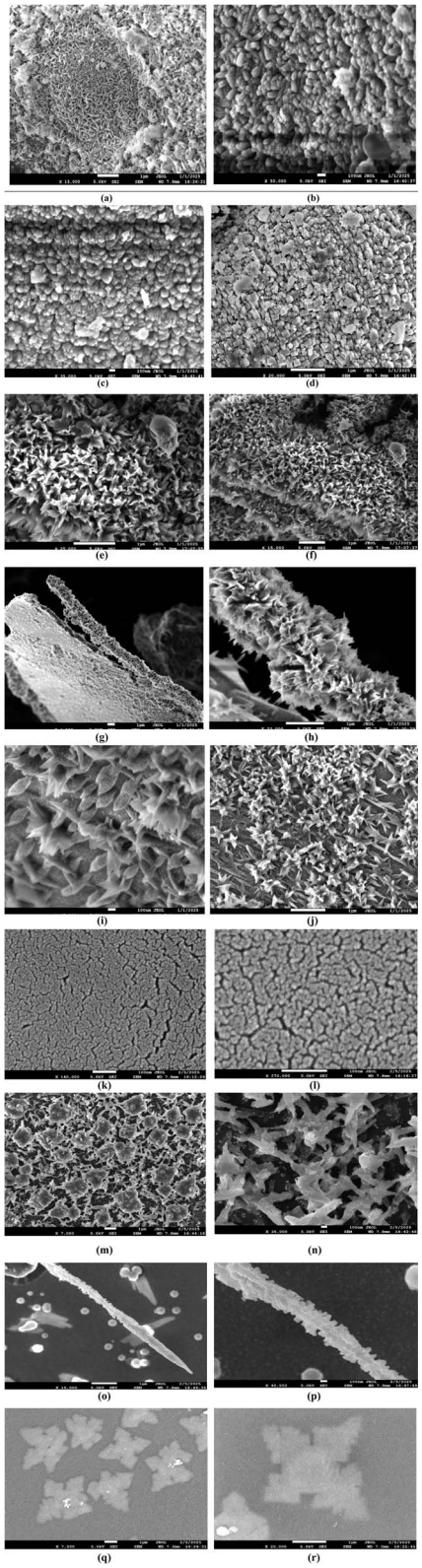

Fig. 8 FESEM images: M2 NPs (a–d), M1 NPs (e–j), Hy (k, l), Hy(M2) (m–p), and Hy(M1) (q, r) samples.

The strong thermal stability of M2 and M1 NP samples in the 30–750 °C temperature range was confirmed by the STA study. The peak at around 750–900 °C was due to an exothermic reaction corresponding to the decomposition of M1 and M2 NPs into a new crystal material.[28] The exothermic reaction of M1 NPs at 750–900 °C has also been confirmed from the DSC curve (Fig. 7c).

3.6. Surface morphology and purity analysis

The surface morphology of the M2 (Fig. 8a–d) and M1 (Fig. 8e–j) NPs was investigated through FESEM studies. The M2 NPs display a flower-shaped surface morphology in Fig. 8a, with the central part presented in Fig. 8b–d, showing needle and star-like shapes with diameters of 20–60 nm. A Similar flower-shaped surface morphology was exhibited by the M1 NPs, as shown in Fig. 8a and b. However, flower rod morphology is observed in Fig. 8g in the case of M1 NPs. The flower shapes are obtained due to the overlap of star- and needle-shaped NPs[66] in the M1 sample, which have diameters of 70–100 nm and are shown in Fig. 8i and j. The surface particle size distribution curves are shown in Fig. 9 for M2 and M1 NP samples, indicating that the particle sizes are 20–60 nm and 70–100 nm for M2 and M1 NPs, respectively.

The 100% purity of the M2 and M1 NPs was found (SI in Table 2) from the EDS (energy-dispersive X-ray spectroscopy) analysis, as shown in SI Figures S1a and S1b, respectively. The carbon (C) and gold (Au) signals in the EDS patterns are obtained due to the carbon tape and gold coating, which provide better resolution for the M2 and M1 NP samples.

Due to its hydrophilicity, the FESEM image of Hy exhibits a net-like structure with pores (Fig. 8k and l). The surface shape of Hy changes dramatically when M1 NPs (Fig. 8m–p) are loaded, and the presence of nanoparticles helps to restore the internal network structure. However, no surface changes are obtained in the case of Hy (M2) (Fig. 8q and r).

3.7. Internal morphology analysis

The internal morphology of the M2 (Fig. 10a–d) and M1 (Fig. 10e–i) NPs was described through HRTEM studies. The M2 NPs exhibit a flower (a mixture of needle and star-like shapes) shaped morphology with diameters of 20–50 nm (Fig. 10a–c), formed due to the overlap of cube-like crystalline particles[67] having diameters of 1–5 nm (Fig. 10d). However, similar flower-shaped M1 NPs are observed with diameters of 70–100 nm (Fig. 10e, g, h, and i). A flower rod morphology of M1 NPs (Fig. 10f) was obtained from internal morphology analysis.

The flower-like surface morphology of both NPs is promising for excellent electrochemical, electronic, and adsorption applications.[68] The FESEM and HRTEM analysis data indicated that the sizes of star- and needle-shapes of M1 NPs are larger in comparison to those of M2 NPs. This may be due to the high calcination temperatures (500 °C) in the case of M2 NPs, where the larger, star- and needle-shaped NPs are broken down into smaller sizes.

3.8. Surface area study by BET

The nitrogen adsorption and desorption isotherms of the M2 and M1 NPs are shown in Fig. 11a and b, respectively. The adsorption and desorption behavior for both materials fits the type IV isotherm with an H2-type hysteresis loop, confirming their mesoporous nature. In M1 NPs, the loop moves to a comparatively higher pressure (P/P_0 = 0.99) with a high volume of adsorption (6.4018 $cm^3\ g^{-1}$ STP). This suggests that, compared to M2 NPs, M1 NPs contain more mesopores. SI Table 3 provides the results of the BET and BJH desorption analyses of the M2 and M1 NP samples. Both BET and BJH desorption surface areas range from 2.5 to 6 $m^2\ g^{-1}$ for both samples. The pore widths in both samples are found to be in the range of 0–30 nm (see the inset of Fig. 11a and b). The BET surface area analysis confirmed the mesoporosity of the M2 and M1 NPs. The BET surface area, BJH desorption surface area, BJH desorption pore volume, and BJH desorption pore radius of the M2 NP samples were lower compared to those of the M1 NP samples.

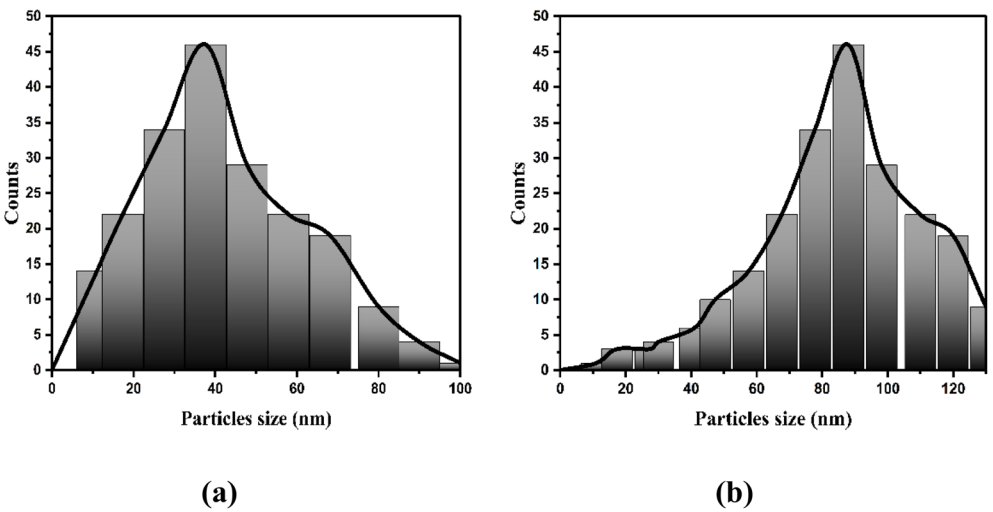

Fig. 9 Surface particle size distribution curve: M2 NPs (a) and M1 NPs (b).

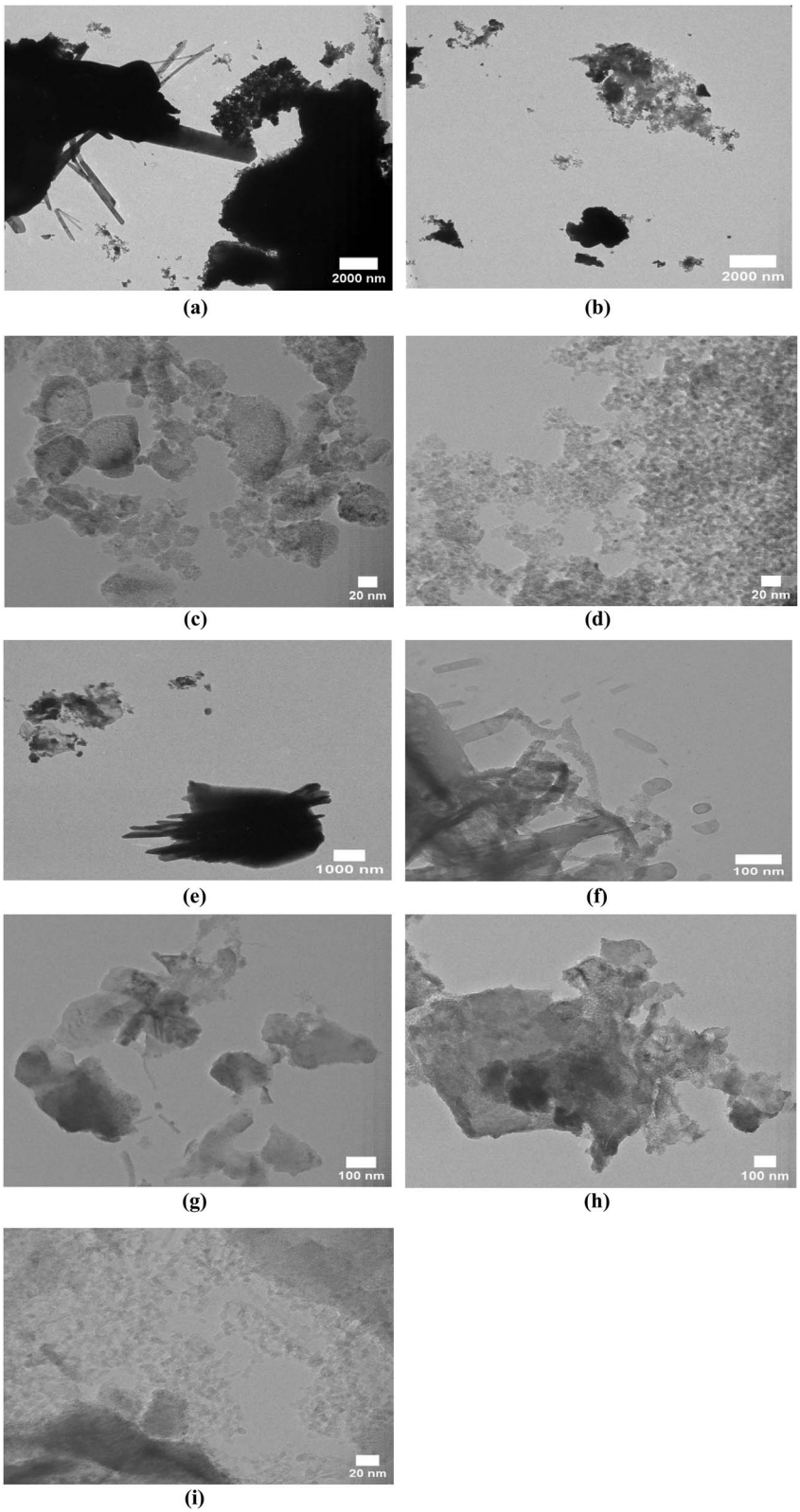

Fig. 10 HRTEM images: M2 (a–d) and M1 (e–i) NP samples.

3.9. Electrochemical analysis

The electrochemical analysis, including cyclic voltammetry (CV), chronopotentiometry (CP), linear sweep voltammetry (LSV), and constant potential electrochemistry (CPE) studies of both NPs in an aqueous sodium hydroxide solution, is shown in Fig. 12 and 13. The CV curves of M1 NPs (Fig. 12a) exhibited supercapacitor-like CV behavior at a scan rate ranging from 50

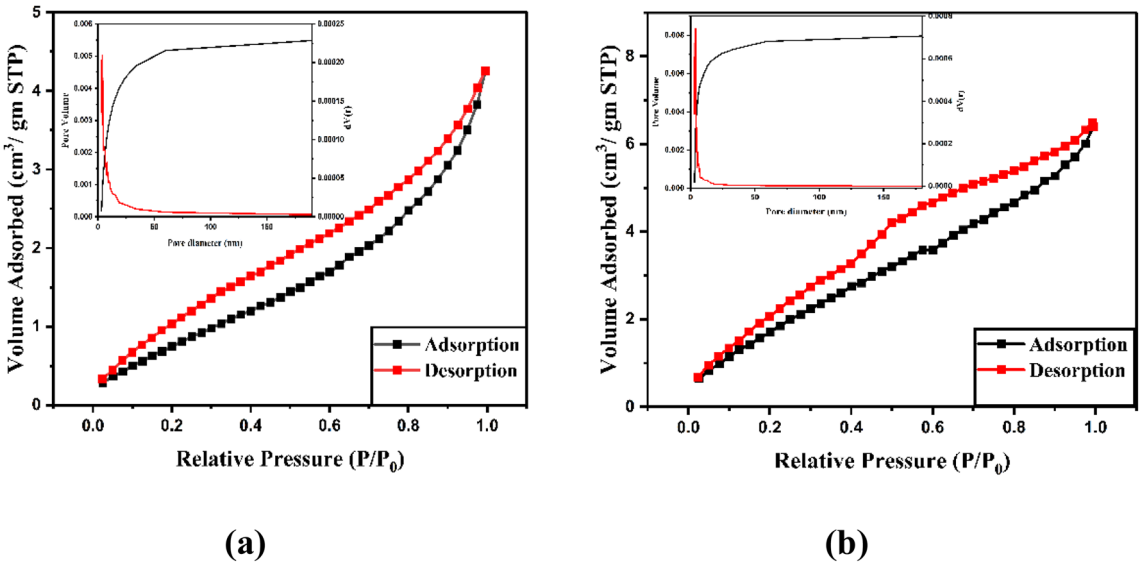

Fig. 11 The nitrogen adsorption and desorption isotherms with pore diameter distribution plots of the (a) M2 NPs and (b) M1 NPs samples.

to 250 mV s^{-1} in a 3 M NaOH aqueous solution. At a higher scan rate, *i.e.*, 300 mV s^{-1}, this material exhibits supercapacitor behavior with slight pseudo-capacitance, as indicated by the CV curves. This CV curve shows that M1 in a 3 M NaOH solution requires a sizable applied potential to increase until the current begins to increase exponentially. Both NPs exhibit a large capacitive or non-faradaic current zone until E_{onset} (Onset potential), where the electrode acts as a capacitor. Once sufficient energy is attained, electron generation and consumption occur at the electrode and electrolyte interfaces, forming the faradaic current zone. The sudden increase in current after E_{onset} signifies the transition from capacitive to battery-type behavior (SI Fig. S2). The CV curves of M1 NPs in a 1 M NaOH solution (Fig. 12b) also exhibit supercapacitor-like pseudo capacitance, similar to the CV curves obtained at scan rates ranging from 50 to 600 mV s^{-1}. The CV curves of the M2 NPs in 3 M (Fig. 12c) and 1 M (Fig. 12d) NaOH solutions correspond to supercapacitors with slight pseudo-capacitance, similar to the CV curves obtained in a 50–600 mV s^{-1} scan rate range. The $E_{oxidation}$ (oxidation potential), $E_{reduction}$ (reduction potential) peaks, and specific capacitance (C_{sp}) data of M2 and M1 NPs for 3 M and 1 M NaOH solutions are tabulated in SI Table 4.

The peak current density significantly decreased when the concentration of NaOH was reduced from 3 M to 1 M. This supports a lower rate of charge transfer, which is similar to that of other metal oxide-based electrodes in alkaline media.[69,70] The variation of anodic and cathodic peak potentials suggests changes in reaction kinetics with higher internal resistance.[71–77] This was comparable to how larger overpotentials in the electrochemical systems resulted from decreased OH^- availability. The broader peaks of the CV curve and smaller enclosed areas demonstrated decreased capacitance.[69,70]

In the case of M1 and M2 NPs in both 1 M and 3 M NaOH solutions, the C_{sp} value (Fig. 12e) decreases with an increase in scan rate due to faster reaction times, but the electrolyte does not have enough time to reach all active electrode sites. Lower scan rates are generally preferred for measuring maximum C_{sp}, as they allow more time for ion diffusion into the electrode.[71–77] Compared to a 3 M NaOH solution, the 1 M solution exhibits a decreased C_{sp} value for M2 NPs at all scan rates (Fig. 12e). A contrasting behavior is observed for the C_{sp} values of M1 NPs in 3 M and 1 M NaOH solutions, *i.e.*, with an increase in electrolyte concentration, the C_{sp} values decrease for 3 M solutions within a 50–500 mV s^{-1} range scan rate. The C_{sp} values are nearly equal for both electrolyte concentrations for M1 NPs at a 600 mV s^{-1} scan rate (Fig. 12e).

The charge storage mechanism in M1 nanoparticles may be influenced by ion diffusion restrictions, surface accessibility, and electrochemical kinetics rather than exhibiting a straightforward double-layer or pseudocapacitive behavior due to concentration effects. While the capacitive response may become more surface-controlled at higher scan rates, producing similar C_{sp} values for both concentrations, the decreased capacitance in 3 M NaOH at lower scan rates may suggest restricted ion penetration due to increased ionic strength.

The CD curve analysis reveals that for samples M1 and M2 NPs in 3 M and 1 M NaOH solutions (Fig. 12f–m), the material retains some of its initial charge, known as the memory effect, even after a discharge time. The source exhibits a nonlinear triangular shape, similar to that of a supercapacitor with pseudo-capacitive behavior. The curve does not exhibit battery-like behavior, with a flat voltage region and a plateau-like shape.[71–77] A small IR drop (/ohmic drop) (where I represents the current and R denotes the resistance) indicates good conductivity (Fig. 12f, g, j and k), while a gradual voltage drop suggests pseudo-capacitive behavior (Fig. 12h, i, l and m).[78]

Linear Sweep Voltammetry (LSV) provides key insights into the electrochemical behavior of the M1 and M2 samples, particularly for the oxygen evolution reaction (OER) and hydrogen evolution reaction (HER).[18,79] The M1 sample exhibited exceptional charge storage and electrocatalytic performance, as evidenced by its reduced overpotential in the OER

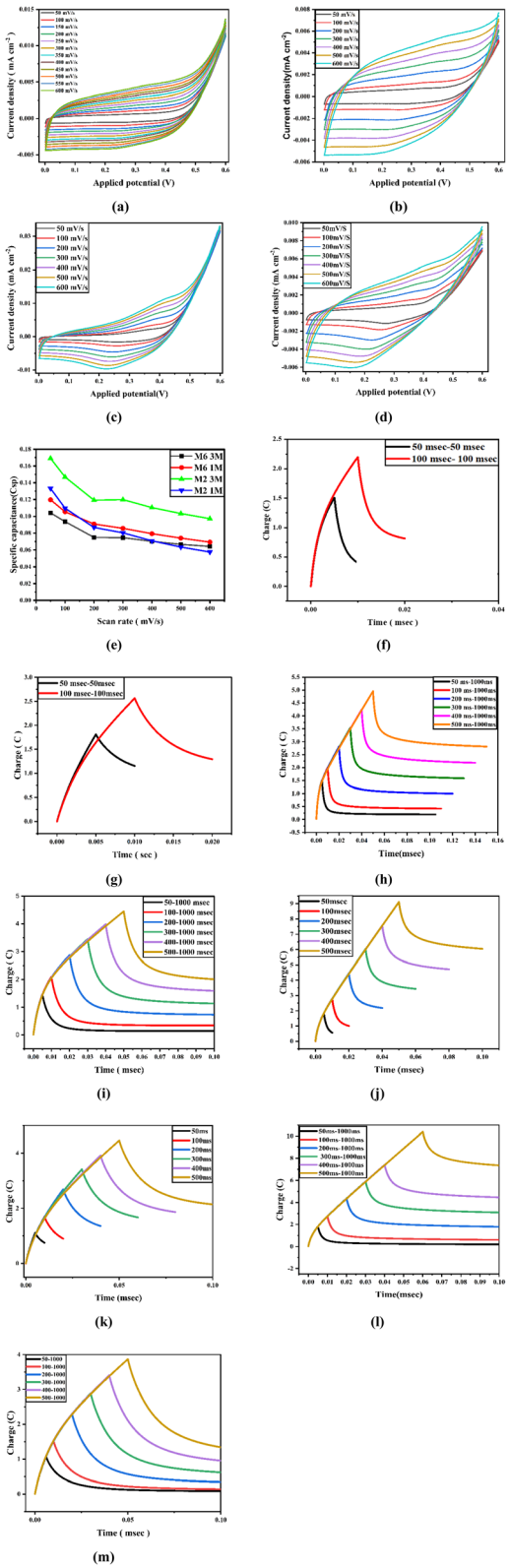

Fig. 12 The CV curves of the M1 NPs sample at 3 M (a), 1 M NaOH (b) solution, and the M2 NP sample in 3 M (c) and 1 M NaOH (d) solution with their C_{sp} values *vs.* scan rate (e). The CD curves of the M1 NP sample for the same time interval in 3 M (f) and 1 M (g) NaOH solution, for the different time intervals in 3 M (h) and 1 M (i) NaOH solution, and also the M2 NP sample for the same time interval in 3 M (j) and 1 M (k) NaOH solution, for the different time intervals in 3 M (l) and 1 M (m) NaOH solution.

and increased specific capacitance, indicating its potential applications in integrated energy storage and conversion. These results indicate that M1 in 3 M NaOH (Fig. 13a and c) is a more effective electrocatalyst for OER and HER applications, showcasing reduced energy demands and enhanced charge transfer rates. In addition, it revealed that the onset potential for M1 in 3 M NaOH (440 mV) was lower than that in 1 M NaOH (480 mV) (Fig. 13b and d), suggesting an increase in catalytic efficiency attributed to the greater availability of OH^- ions. The increased electrolyte concentrations improved OER performance by promoting quicker charge transfer kinetics.[18,79] The faradaic zone significantly expanded with the increasing scan rate (50–600 mV s^{-1}), suggesting increased redox contributions. These results are similar to those observed in hybrid electrochemical materials, indicating that zirconium ferrite NPs exhibit capacitive and battery-like charge storage behavior.[18,79]

In contrast to 1 M NaOH (−1255 mV), the HER onset potential for M1 in 3 M NaOH (−1200 mV) was less negative, suggesting enhanced catalytic activity at higher electrolyte concentrations. Similarly, M2 NPs (Fig. 13e and f) showed more negative onset potentials in both electrolytes compared to M1 NPs, possibly due to less HER activity. These are consistent with increased overpotentials resulting from decreased charge transfer efficiency at lower electrolyte concentrations.[18,79]

Chronopotentiometry (CPE) measures the current response when a constant voltage is applied to investigate the long-term stability and endurance of electrocatalysts. Through the identification of appropriate potential ranges for stability testing, LSV (Linear Sweep Voltammetry) aids in CPE. LSV determines the overpotential needed for a given current density (10 mA cm^{-2} for OER or −10 mA cm^{-2} for the HER) to ensure that CPE is carried out under realistic operating circumstances. By tracking voltage drift, CPE data shed light on catalyst stability; if the potential remains constant over time, the material is robust; if it rises, degradation occurs. CPE for M1 and M2 in 1 M *versus* 3 M NaOH demonstrates how electrolyte concentration affects stability; the more negligible drift in 3 M NaOH indicates improved ionic conductivity and long-term performance. The CPE data show steady potential over a long period and strong catalyst durability (Fig. 13i–l).

The CV and CD analysis confirmed that the supercapacitor exhibited pseudo-capacitive behavior in the M2 NP samples in NaOH solutions (both 1 M and 3 M). The M1 NP samples show pseudo-capacitive behavior only in 1 M NaOH solution and a combination of capacitive and pseudo-capacitive behavior in 3 M NaOH solution, functioning as fractional order supercapacitors in electronic application. Long-term electrochemical performance is enhanced in concentrated alkaline media due to higher ionic conductivity. The electrode's ability to sustain a constant reaction rate confirms the continuous production of H_2 and O_2 during the HER and the OER.[18,79]

3.10. Electronic analysis

3.10.1. Experimental analysis of the fractional order supercapacitor using M2 and M1 NPs. The impedance analysis of the proposed supercapacitor model using both NPs was

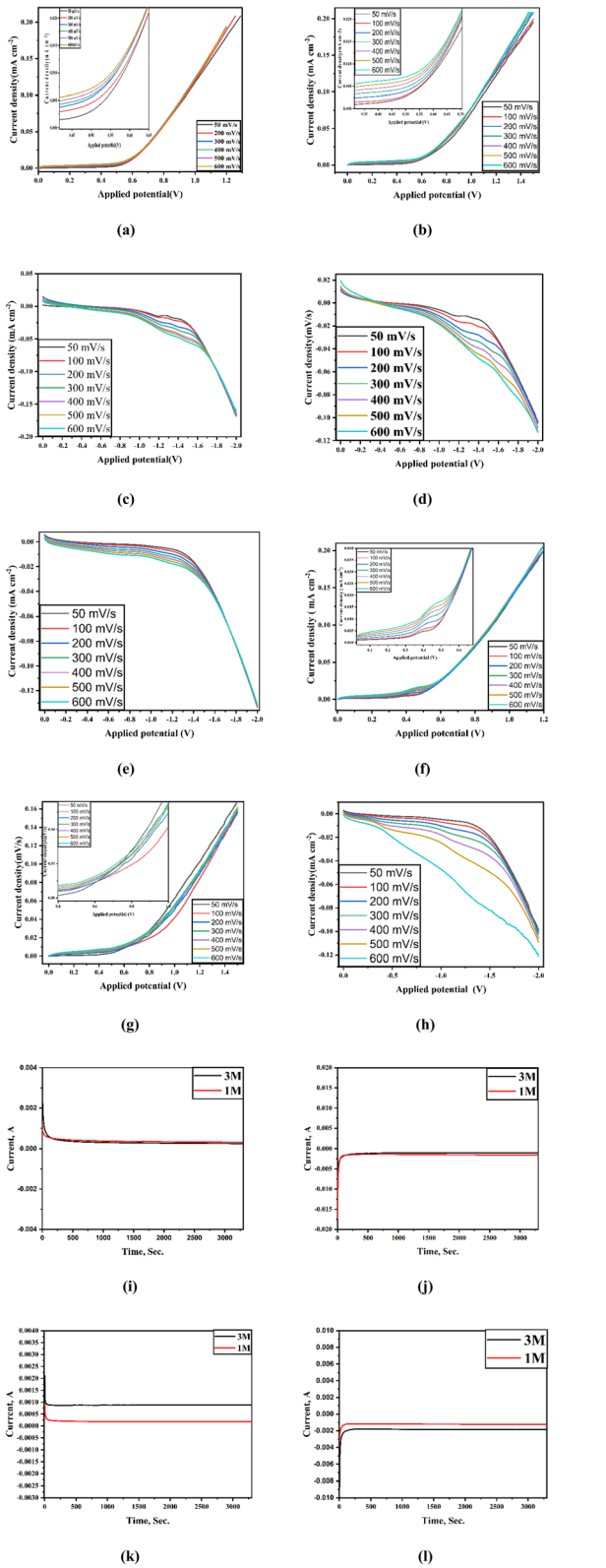

Fig. 13 The LSV curves at different NaOH concentrations: (1) M1 NP sample (the +ve potential) – (a) 3 M and (b) 1 M; for −ve potential – (c) 3 M and (d) 1 M. (2) M2 NP sample (the +ve potential) – (e) 3 M and (f) 1 M; for the −ve potential – (g) 3 M and (h) 1 M. The CPE curves at 1 M and 3 M NaOH concentrations: M1 NP sample – (i) +ve potential and (j) −ve potential.; M2 NP sample – (k) +ve potential, and (l) −ve potential.

performed using a Tektronix TBS 2000 series 100 MHz digital storage oscilloscope (DSO) and a Tektronix AFG1022 20 MHz function generator. An input voltage of 5 V was provided from a frequency range of 100 Hz to 20 MHz, and the corresponding impedance analysis was conducted. There was no significant change in the magnitude of V_0/V_{in} with respect to the input voltage, ranging from 1 V to 5 V.

The proposed capacitor model provides the magnitude and phase responses, as shown in Fig. 14a and b. The phase characteristics of M1 NPs show a constant phase (CP) behavior of −15° over a functional frequency range of 10^3 Hz to 10^5 Hz. On the other hand, M2 shows a more resistive type behavior, with phase values ranging from 0° to −4°. Unlike M2, the magnitude of M1 shows some unreal characteristics; therefore, capacitance was determined across varying frequencies. The model fabricated using M2 does not qualify as a capacitor due to its low phase shift and nearly zero magnitude. It was observed, as shown in Fig. 14c, that the capacitance value decreases as the frequency increases and remains within the range of 1–1.5 F within the CP functional frequency range. From the phase characteristics, it is confirmed to behave as a fractional capacitor; therefore, the variations of fractional order (α)[80] concerning frequency have been reported in Fig. 14d.

The fractional-order supercapacitor reveals its unique frequency-dependent characteristics, highlighting its behavior as a non-ideal capacitor with fractional-order dynamics. The capacitance plot indicates a peak value of approximately 1.5 F $s^{-1-\alpha}$ in mid-frequency ranges (10^5 to 10^6 Hz), followed by a decline at higher frequencies, demonstrating a frequency-dependent capacitance consistent with fractional-order behavior. The phase plot, which decreases from approximately −10° to −40° across the frequency range, confirms its fractional-order nature, with a constant phase angle deviation indicative of a fractional-order parameter ($\alpha = 0.16$).[80] This characteristic phase lag and frequency-dependent capacitance enable the supercapacitor to exhibit memory effects and non-local behaviors (Fig. 14e), making it suitable for applications that require precise control of reactive power and harmonic suppression. These properties enhance its potential for advanced energy storage and power electronics, particularly in dynamic systems and harmonic-rich environments.

3.10.2. FSC-based harmonic filters for power factor correction. Fractional-order capacitors (FOCs) significantly enhance power factor correction (PFC) by offering frequency-dependent impedance that enables precise reactive power compensation and harmonic suppression across a wide frequency range. Unlike traditional integer-order capacitors, which are optimized for single frequencies, FOCs adapt dynamically to varying loads, minimizing overcompensation or undercompensation. Their inherent memory effects and fractional-order resonance make them highly effective in mitigating harmonics, reducing total harmonic distortion (THD), and improving power quality. However, FOCs exhibit resistive-like behavior at specific frequencies, leading to additional energy dissipation as heat. This reduces overall energy efficiency in systems where minimal power loss is critical. In this case, a fractional-order supercapacitor comes into account,

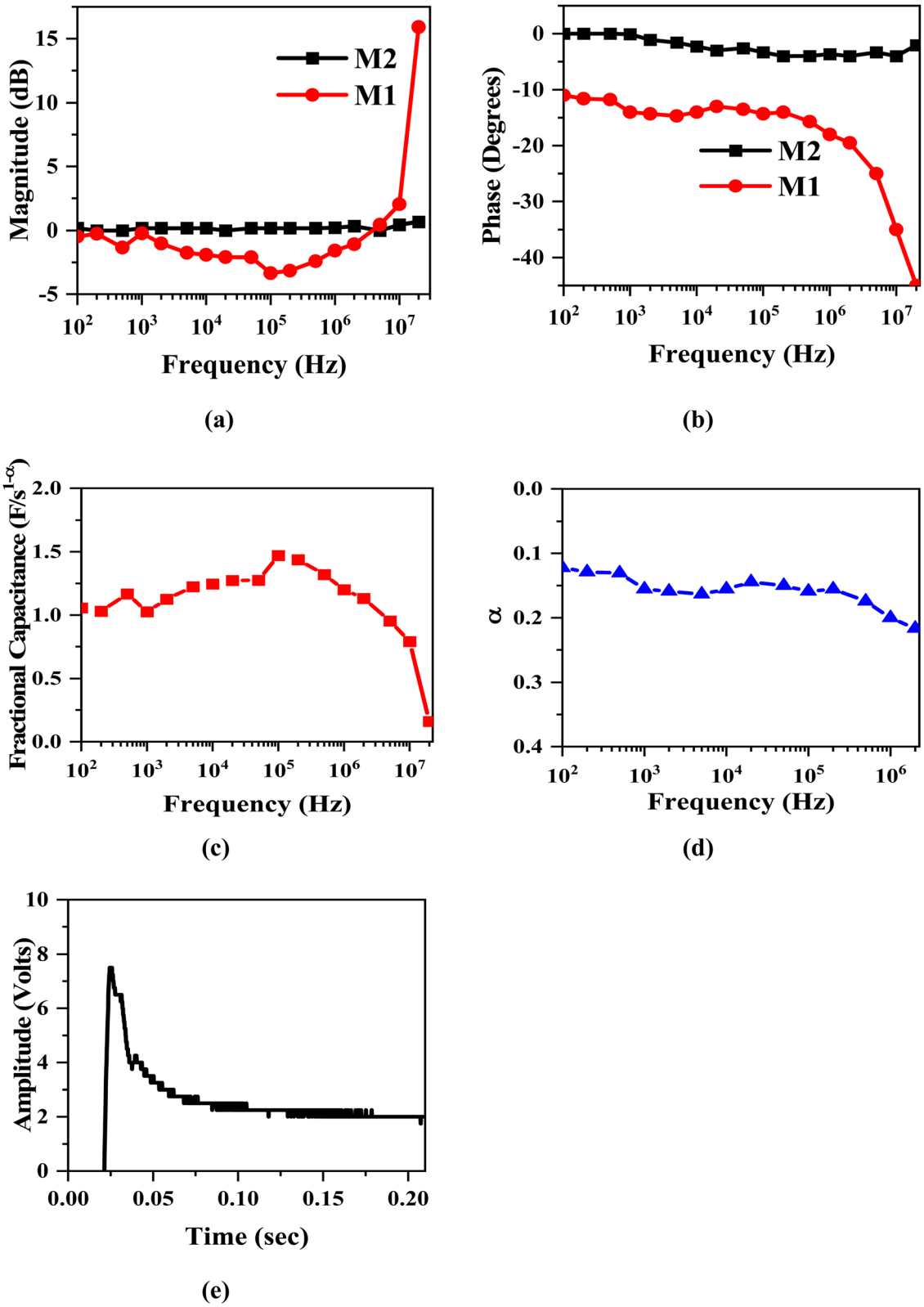

Fig. 14 (a an b) Experimental frequency domain analysis of M2 and M1 NP-based fractional-order supercapacitors. Experimental analysis of (c) fractional capacitance and (d) fractional order concerning the frequency of the M1 sample in the proposed fractional-order supercapacitor. (e) Charging and discharging of the proposed (M1) fractional-order supercapacitor.

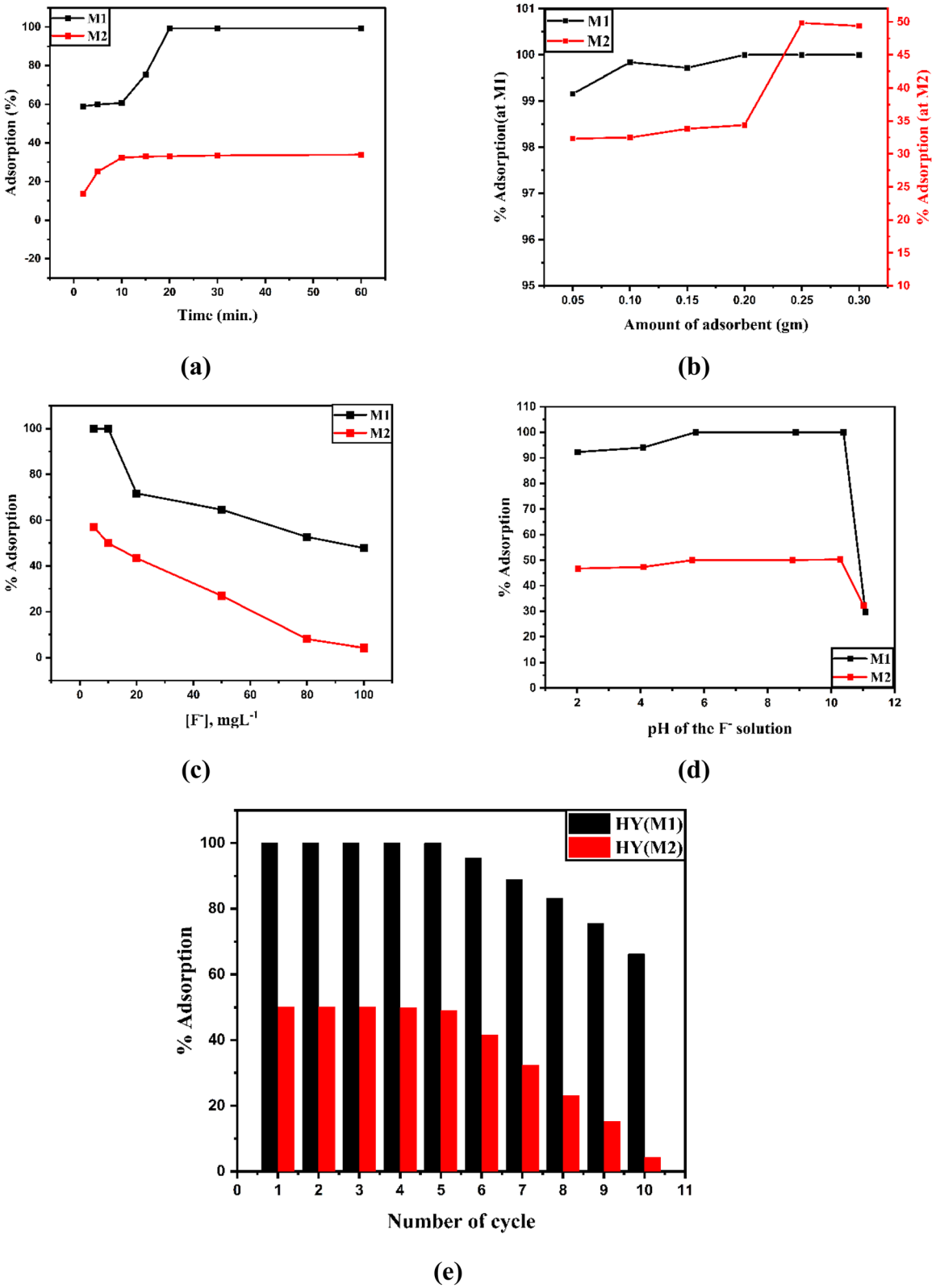

Fig. 15 Adsorption of F^- ions in 20 mL solutions: for M2 and M1 NPs as adsorbents – (a) variation of time, (b) amount of adsorbents, (c) concentration of F^- ions, and (d) pH variation; For Hy(M2) and Hy(M1) membranes – (e) the number of adsorption cycles.

where the frequency-dependent capacitance compensates for the loss that is encountered due to the resistive component $\cos\left(\frac{\alpha\pi}{2}\right)\omega^{\alpha}$.

The circuit diagram of the fractional-capacitor-based harmonic notch filter is shown in SI Fig. S3a, whereas the frequency domain analysis is reported in SI Fig. S3b, as obtained from the MATLAB simulations. A harmonic notch filter tuned to a center frequency of 50 Hz can effectively serve as a power factor correction (PFC) circuit by suppressing harmonic currents and compensating reactive power. It allows the fundamental frequency to pass with minimal attenuation while blocking higher-order harmonics (*e.g.*, 150 Hz, 250 Hz) and frequencies within the −3 dB bandwidth around 50 Hz. This improves current waveform quality, reduces total harmonic distortion (THD), and aligns the current phase with the voltage, enhancing the power factor. The experimental setup of the harmonic notch filter is depicted in SI Fig. S4a, and its magnitude frequency response is shown in SI Fig. S4b. Here, the response indicates that the experimentally obtained results closely align with the simulated ones. By bypassing harmonic currents and preventing them from flowing back into the source, the filter improves system efficiency, reduces losses, and ensures compliance with power quality standards, making it vital for modern power systems.

3.11. Reservoir of F^- ions

The adsorbent efficiency of M2 and M1 was evaluated for fluoride ions (F^-). The effect of contact time (Fig. 15a) was the primary focus of the adsorption studies, in which 0.05 g of M2 and M1 samples per 20 mL of 10 ppm fluoride ion solution were added for up to 1 h. The initial findings demonstrated that while adsorption is initially rapid, it eventually slows down to attain saturation. In just 10 min, M2 demonstrated ≈33% adsorption, and M1 demonstrated ∼100% in 20 minutes. At 30 min, there was no significant change in % adsorption in both cases with respect to the same at 10 min and 20 min for M2 and M1 NPs, respectively, indicating a state of equilibrium. Hence, the saturation times for fluoride ion adsorption by M2 and M1 are 10 and 20 min, respectively.

The amount of adsorbent used is a key factor in quantifying its adsorption capacity from a fluoride ion solution. When the amount of adsorbent increases, the percentage of fluoride ions removed through adsorption and the number of adsorption sites also increase. The ability of the adsorbent to adsorb the least amount and its cost-effectiveness are studied. The effect of the amount of adsorbent (Fig. 15b) is studied by varying the amounts of M2 (Fig. 15a) and M1 (Fig. 15b) in a 20 mL solution of 10 ppm fluoride ions for up to 10 min and 20 min, respectively. The decrease in the concentration of fluoride ion solution (10 ppm in 20 mL) with varying amounts of adsorbent M2 and M1 is shown in Fig. 15b.

In the present study, the M2 sample exhibited 33% initial adsorption at 0.05 g, which increased to 50% at 0.25 g, and reached saturation above this dosage. Hence, the optimized dose for the M2 adsorbent is 0.25 g per 20 mL of a 10 ppm fluoride ion solution for 10 min at room temperature. Similarly, the M1 sample achieved 99% initial adsorption at 0.05 g which enhanced to 100% at 0.2 g. After 20 min at room temperature, the optimal dose of M1 was 0.2 g per 20 mL of a 10 ppm fluoride ions solution. From an economic perspective, this increase is significant; therefore, using M1 adsorbents at 0.2 g per 20 mL of a 10 ppm fluoride ion solution would be the best course of action, *i.e.*, achieving 100% removal of the fluoride ions.

The number of accessible sites on an adsorbent surface directly affects the initial adsorption of fluoride ions. Saturation of adsorption sites causes the percentage of adsorption or removal to decrease as the concentration of initial fluoride ions increases. However, the high driving force for mass transfer extends the capacity of the adsorbents. Fig. 15c illustrates the influence of fluoride ion concentrations in the 5–100 ppm range on its absorption; however, at 100 ppm, it reaches saturation at 48% for M1 and 4.2% for M2 adsorbents. The impact of pH ($2 \leq pH \leq 11$) on the adsorption of 10 ppm of fluoride ions by the

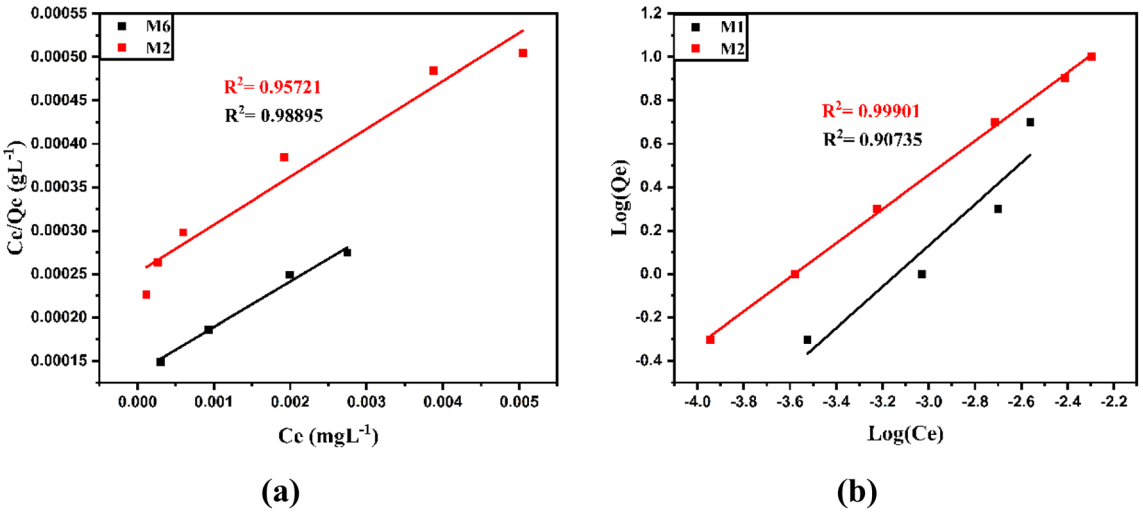

Fig. 16 (a) Langmuir and (b) Freundlich adsorption isotherm study of adsorption of F^- ions using M2 and M1 NPs as adsorbents.

optimal quantity of M2 and M1 samples was investigated. The results (Fig. 15d) showed that in a pH range of 1–10, fluoride ions adsorption is almost constant at ~100% for M1 NPs, ~50% for M2 NPs, and slightly decreases or saturates with raising the pH to 11. This is most likely because the fluoride ions are drawn towards the M2 and M1 samples due to their surface charges within the pH range of 1–10.

The Hy membranes do not adsorb fluoride ions. Fluoride ion adsorption was conducted for 10 cycles to ascertain the heterogeneity of the composite adsorbents, Hy(M2) and Hy(M1) membranes (Fig. 15e), in a 20 mL solution of 10 ppm fluoride ions for 20 min. Furthermore, the percentage of adsorption of the fluoride ions in the case of Hy(M1) is higher than that of Hy(M2) across all cycles, indicating that Hy(M1) is a better reservoir of fluoride ions than Hy(M2). The Hy(M1) adsorbed fluoride ions at ~100% up to 6 cycles; thereafter, the efficiency decreased to ~70% at 10 cycles.

3.11.1. Adsorption isotherm analysis. The Langmuir and Freundlich isotherms are two of the most widely used models for assessing adsorption effectiveness. These models describe the distribution of adsorbate molecules between the liquid phase and the solid surface at equilibrium.[16]

An empirical model that considers adsorption onto a heterogeneous surface with several active sites of different energies is the Freundlich isotherm (SI as E2) (shown in Fig. 16b). The equilibrium concentration of the adsorbate in solution is C_e (mg L^{-1}). The adsorbed quantity per unit mass of the adsorbent is denoted by Q_e (mg g^{-1}), while the adsorption capacity and intensity are indicated by the Freundlich constants k_F and n, respectively. The graph of $\ln(Q_e)$ *versus* $\ln(C_e)$ is a straight line whose slope and intercept yield k_F and $1/n$, supporting that higher adsorption occurs at lower concentrations.

The Langmuir isotherm, on the other hand, assumes that monolayer adsorption occurs on a uniform surface with adsorption sites (SI as E3) (shown in Fig. 16a). The maximum adsorption capacity when a monolayer covers the surface is indicated by Q_{max} (mg g^{-1}). The Langmuir constant linked to adsorption energy is k_L (L g^{-1}). Q_{max} and k_L values are obtained from a plot of C_e/Q_e *versus* C_e. Furthermore, the feasibility of adsorption is determined by the equilibrium parameter R_L (SI as E4), where C_0 is the starting adsorbate concentration and a_L (= k_L/Q_{max}) is a Langmuir constant. The adsorption process is divided into three categories: irreversible adsorption ($R_L = 0$), unfavorable or linear adsorption ($R_L > 1$), and favorable adsorption ($R_L < 1$).

The Freundlich and Langmuir models (Table 3) adequately describe the adsorption behavior; however, the Langmuir model offers a more potent connection based on statistical factors. The M1 NPs have a considerably higher Q_{max} value than M2 NPs in the Langmuir adsorption isotherm model, indicating that the former is a more effective adsorbent for adsorbing F^- ions. The Hy(M1) is an efficient reservoir of F^- ions.

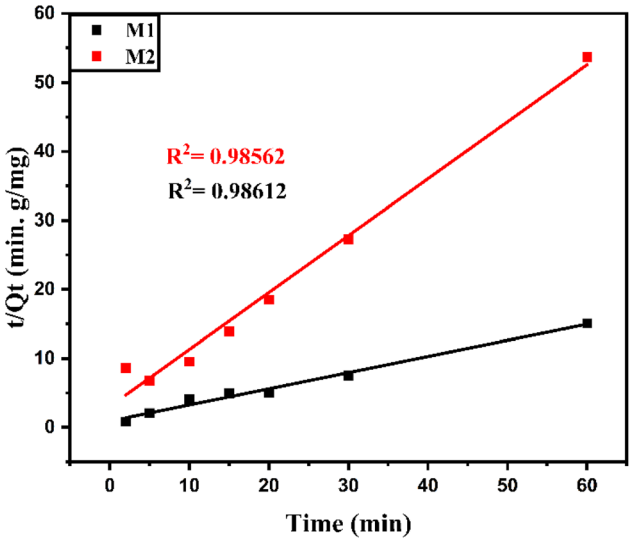

Fig. 17 Linear pseudo-second-order kinetics study of adsorption of F^- ions using M2 and M1 NPs as adsorbent.

Table 4 Linear pseudo-second-order kinetics model data of the adsorption of F^- ions

Absorbent	k_2 (g mg^{-1} min^{-1})	Q_e (mg g^{-1})	R^2
M1	0.05891	4.27223	0.98612
M2	0.22404	1.21181	0.98562

3.11.2. Adsorption kinetics study. The linear versions of the pseudo-second-order kinetics model (SI, E5) (Fig. 17) were used to investigate the rate and mechanism of F^- ion adsorption on M2 NPs and M1 NPs. The pseudo-second-order rate constant is k_2 (g mg^{-1} min^{-1}), Q_t (mg g^{-1}) is the amount adsorbed at time t, and Q_e (mg g^{-1}) is the equilibrium adsorption capacity. Important kinetic parameters, including the initial adsorption rate (h), the equilibrium adsorption capacity (Q_e), the amount adsorbed at time t (Q_t), and the pseudo-second-order rate constants k_2 (g^{-1} mg min), can all be experimentally determined by plotting t/Q_t *versus* t (given in Table 4). The pseudo-second-order kinetics model (linear) provides a good fit for M2 and M1 NPs, indicating that the adsorption process is likely governed by chemisorption, which involves electron transfer between the adsorbent and the adsorbate.

Table 3 Langmuir and Freundlich adsorption isotherm data of the adsorption of F^- ions

	Langmuir					Freundlich		
Absorbent	a_L (L mg^{-1})	K_L (L g^{-1})	Q_{max} (mg g^{-1})	r_L^2	R_L	K_F	$1/n$	r_F^2
M1	20.03	383	19.11	0.98895	0.00989	651	0.950	0.90735
M2	12.11	219	18.12	0.95721	0.01625	651	0.786	0.99901

4. Conclusion

This study focused on the synthesis of zirconium ferrite NPs and investigated their surface characteristics, composition, and purity in a composite of Hy membranes. XRD and XPS data confirm the existence of 100% pure $ZrFe_2O_5$ nanoparticles. The band gap energy of the zirconium ferrite NPs increased with an increase in calcination temperature, *i.e.*, higher for M2 NPs in comparison to M1 NPs. The robust thermal stability of M2 and M1 NP samples was validated by STA analysis at temperatures ranging from 30 to 750 °C. The flower-like surface shape of both NPs is advantageous for electrochemical, electrical, and adsorption applications. The M1 NP samples demonstrated a combination of supercapacitors and supercapacitors with pseudo-capacitive behavior in 3 M NaOH solution, functioning as fractional-order supercapacitors in electronic applications. The electrode's capacity to maintain a stable reaction rate validates the continuous generation of H_2 and O_2 during the HER and OER. The Freundlich and Langmuir models effectively represented adsorption behavior, although the Langmuir model demonstrated a more robust correlation. M1 NPs exhibit a higher Qmax value than M2 NPs, signifying their effectiveness in removing F^- ions through adsorption, with the Hy(M1) membrane serving as an effective reservoir of F^- ions.

The engineered fractional-order supercapacitor may be utilized in future real-time power factor correction circuit research.

Author contributions

The conceptualization and design of the study were provided by A. N. A. and A. S. The interpretation of data was performed by A. N. A. The manuscript was prepared by A. N. A. and A. S. The fractional-order supercapacitor was designed by A. N. A. and A. S., and its properties were observed by S. S. and M. C. T. All other authors supported this work.

Conflicts of interest

The authors declared no conflict of interest.

Data availability

The data supporting the findings of this investigation are accessible from the corresponding author upon reasonable request.

Equations E1 to E5, Fig. S1 to S4, and Tables 1 to 8 are submitted as the SI. See DOI: **https://doi.org/10.1039/d5na00578g**.

Acknowledgements

In honour of Professor Anadi Charan Dash, former Professor of Chemistry, Utkal University, Bhubaneswar, for his dedicated research in India. The XRD, FESEM, EDS, and HRTEM characterization studies were conducted with the support of the Department of Chemistry, ICT-IOC, Bhubaneswar, India. The XPS characterization was performed with the assistance of the National Chemical Laboratory (NCL), Mumbai, India. The authors express their appreciation for the assistance in characterizing zirconium ferrite NPs.

References

1 L. Zhou, J.-Y. Zhang, X.-Q. Zhu, D.-M. Xu and S.-S. Zheng, *J. Cleaner Prod.*, 2024, **471**, 143358.
2 K. W. Borth, C. W. Galdino, V. de C. Teixeira and F. J. Anaissi, *Appl. Surf. Sci.*, 2021, **546**, 149126.
3 L. Wei and Z. Gao, *RSC Adv.*, 2023, **13**, 8427–8463.
4 D. Mohan, C. U. Pittman and P. H. Steele, *J. Colloid Interface Sci.*, 2006, **297**, 489–504.
5 G. Zhao, J. Zou, X. Chen, L. Liu, Y. Wang, S. Zhou, X. Long, J. Yu and F. Jiao, *Chem. Eng. J.*, 2021, **421**, 127845.
6 A. S. Al-Wasidi, E. A. Abdelrahman, K. ur Rehman, F. A. Saad and A. M. Munshi, *Sci. Rep.*, 2024, **14**, 29599.
7 R. W. Premathilaka and N. D. Liyanagedera, *J. Nanotechnol.*, 2019, **2019**, 1–15.
8 A. Hota, S. G. K. Patro, S. K. Panda, M. A. Khan, M. A. Hasan, S. Islam, M. Alsubih, N. A. Khan and S. Zahmatkesh, *J. Water Process Eng.*, 2024, **58**, 104776.
9 N. S. Al-Kadhi, G. M. Al-Senani, F. A. Saad, A. M. Munshi and E. A. Abdelrahman, *Sci. Rep.*, 2024, **14**, 27973.
10 N. S. Al-Kadhi, E. A. Abdelrahman, F. S. Alamro, R. K. Shah, F. A. Saad and K. ur Rehman, *Sci. Rep.*, 2025, **15**, 4153.
11 W. A. Khoso, N. Haleem, M. A. Baig and Y. Jamal, *Sci. Rep.*, 2021, **11**, 3790.
12 P. Pillai, S. Dharaskar, S. Sasikumar and M. Khalid, *Appl. Water Sci.*, 2019, **9**, 150.
13 F. W. F. de Oliveira, S. C. dos Reis, L. S. Ribeiro, L. N. M. Velásquez, A. A. C. Cotta, V. L. dos Santos, P. L. Gastelois, J. D. Ardisson and A. Santos, *Environ. Technol. Innovation*, 2021, **24**, 101995.
14 J. Yu, J. Huang, R. Li, Y. Li, G. Liu and X. Xu, *Nat. Commun.*, 2025, **16**, 361.
15 J. P. Dhal, A. Sahoo and A. N. Acharya, *Emerging Mater. Res.*, 2023, **12**, 136–144.
16 A. Sahoo, P. Jena, J. Behera and A. N. Acharya, *ChemistrySelect*, 2024, **9**, e202402393.
17 A. ur Rehman, M. Ahmad, S. Hassan, S. Q. Hussain, M. W. Iqbal and H. E. Ali, *Mater. Chem. Phys.*, 2023, **295**, 127165.
18 N. M. Malima, M. D. Khan, S. C. Masikane, F. M. de Souza, J. Choi, R. K. Gupta and N. Revaprasadu, *Sci. Rep.*, 2023, **13**, 22179.
19 A. Fatima, H. Aldosari, M. S. Al-Buriahi, M. Al Huwayz, Z. A. Alrowaili, M. S. Alqahtani, M. Ajmal, A. Nazir, M. Iqbal, R. Tur Rasool, S. Muqaddas and A. Ali, *ACS Omega*, 2023, **8**, 37927–37935.
20 J. Wei, Y. Shao, J. Xu, F. Yin, Z. Li, H. Qian, Y. Wei, L. Chang, Y. Han, J. Li and L. Gan, *Nat. Commun.*, 2024, **15**, 9012.
21 A. Saad, Y. Gao, K. A. Owusu, W. Liu, Y. Wu, A. Ramiere, H. Guo, P. Tsiakaras and X. Cai, *Small*, 2022, **18**, 2104303.
22 X. Xiao, L. Yang, W. Sun, Y. Chen, H. Yu, K. Li, B. Jia, L. Zhang and T. Ma, *Small*, 2022, **18**, 2105830.

23 N. C. Hildebrandt, J. Soldat and R. Marschall, *Small*, 2015, **11**, 2051–2057.
24 P. Thiyagarajan, H. Ahn, J. Lee, J. Yoon and J. Jang, *Small*, 2013, **9**, 2341–2347.
25 K. Ye, Y. Zhang, S. Mourdikoudis, Y. Zuo, J. Liang and M. Wang, *Small*, 2023, **19**, 2302341.
26 P. Agale, V. Salve, K. Patil, S. Mardikar, S. Uke, S. Patange and P. More, *Ceram. Int.*, 2023, **49**, 27003–27014.
27 S. P. Patil and S. A. Jagadale, in *Spinel Ferrite Nanostructures for Energy Storage Devices*, Elsevier, 2020, pp. 123–145.
28 B. Jeevanantham, M. K. Shobana, T. Pazhanivel and H. Choe, *J. Alloys Compd.*, 2023, **960**, 170651.
29 B. Debnath, S. Parvin, H. Dixit and S. Bhattacharyya, *ChemSusChem*, 2020, **13**, 3875–3886.
30 A. Fatima, H. Aldosari, M. S. Al-Buriahi, M. Al Huwayz, Z. A. Alrowaili, M. S. Alqahtani, M. Ajmal, A. Nazir, M. Iqbal, R. Tur Rasool, S. Muqaddas and A. Ali, *ACS Omega*, 2023, **8**, 37927–37935.
31 M. Li, Y. Xiong, X. Liu, X. Bo, Y. Zhang, C. Han and L. Guo, *Nanoscale*, 2015, **7**, 8920–8930.
32 K. Patil, S. Kadam, P. Lokhande, S. Balgude and P. More, *Solid State Commun.*, 2021, **337**, 114435.
33 V. Salve, P. Agale, A. Rokade, M. Kamble, S. Patange and P. More, *New J. Chem.*, 2023, **47**, 20653–20667.
34 S. Gupta, S. B. Carrizosa and B. Aberg, *Sci. Rep.*, 2024, **14**, 29277.
35 T. J. Freeborn, B. Maundy and A. S. Elwakil, *Mater. Renew. Sustain. Energy.*, 2015, **4**, 1–7.
36 K. H. Kenari, A. Bahari and M. S. Lashkenari, *J. Energy Storage*, 2023, **74**, 109274.
37 A. Allagui and A. S. Elwakil, *Sci. Rep.*, 2021, **11**, 13306.
38 R. Balasubramaniam, A. V. Ramesh Kumar and P. Dillmann, *Curr. Sci.*, 2003, **85**, 1546–1555.
39 H. Zhang, N. Du, S. Wang, Q. Zhao and W. Zhou, *Materials*, 2020, **13**, 726.
40 S. B. Babar, N. L. Gavade, H. Shinde, P. G. Mahajan, K. H. Lee, N. Mane, A. Deshmukh, K. M. Garadkar and V. M. Bhuse, *ACS Appl. Nano Mater.*, 2018, **9**, 4682–4694.
41 J. P. Engle, *Corrosion*, 1978, **34**, 301–303.
42 G. Svehla, *Anal. Chem.*, 1997, **343**, 240–245.
43 J. Tian, M. Ernst, F. Cui and M. Jekel, *Desalination*, 2013, **320**, 40–48.
44 G. Dalei, S. Das and A. N. Acharya, *J. Mater. Sci.*, 2025, **60**, 2131–2150.
45 V. Singh, S. Kuthe and N. V. Skorodumova, *Batteries*, 2023, **9**, 184.
46 I. Shitanda, M. Komoda, Y. Hoshi and M. Itagaki, *Analyst*, 2015, **140**, 6481–6484.
47 A. Mukherjee, M. K. Adak, S. Upadhyay, J. Khatun, P. Dhak, S. Khawas, U. K. Ghorai and D. Dhak, *ACS Omega*, 2019, **4**, 9686–9696.
48 S. A. Shahid, A. Nafady, I. Ullah, Y. H. Taufiq-Yap, I. Shakir, F. Anwar and U. Rashid, *J. Nanomater.*, 2013, **2013**, 517643.
49 N. Kaur, A. Katoch, S. Singh and R. Kaur, *Mater. Lett.*, 2023, **330**, 133236.
50 Y. Ahmadian, A. Bakravi, H. Hashemi and H. Namazi, *Polym. Bull.*, 2019, **76**, 1967–1983.
51 S. Arade, P. Agale, S. Balgude, S. Patange, D. Hingane and P. More, *Inorg. Chem. Commun.*, 2024, **170**, 113170.
52 F. Z. Hammadi, M. S. Belardja, M. Lafjah and A. Benyoucef, *J. Inorg. Organomet. Polym. Mater.*, 2021, **31**, 1176–1184.
53 S. Sambyal, A. Singh, R. Tickoo, A. Goswami, S. Kumar and M. Singh, *Phys. Rev. B: Condens. Matter Mater. Phys.*, 2024, **691**, 416357.
54 Z. Azdad, L. Marot, L. Moser, R. Steiner and E. Meyer, *Sci. Rep.*, 2018, **8**, 16251.
55 S. Sagadevan, J. A. Lett and I. Fatimah, *Sci. Technol. Indones*, 2023, **8**, 585–593.
56 A. Arjun, A. Dharr, T. Raguram and K. S. Rajni, *J. Inorg. Organomet. Polym. Mater.*, 2020, **30**, 4989–4998.
57 M. Parastar Gharehlar, S. Sheshmani, F. R. Nikmaram and Z. Doroudi, *Sci. Rep.*, 2024, **14**, 4625.
58 J. Gao, F. Huang, W. Yuan, J. Cheng, H. Huang, J. Zhang, F. Yi, H. Zhang and S. Feng, *Water, Air, Soil Pollut.*, 2021, **232**, 329–336.
59 Y. Hussein, E. A. Kamoun, S. A. Loutfy, R. Amin, E. M. El-Fakharany, T. H. Taha and M. Amer, *J. Umm Al-Qura Univ. Appl. Sci.*, 2023, **9**, 304–316.
60 G. H. Matar and M. Andac, *Polym. Bull.*, 2021, **78**, 6095–6113.
61 A. R. Jamali, A. A. Shaikh and A. D. Chandio, *Preprints*, 2023, 1–13.
62 M. B. Thürmer, C. E. Diehl, F. J. B. Brum and L. A. dos Santos, *Mater. Res.*, 2014, **17**, 109–113.
63 A. Sahoo and A. N. Acharya, *Sens. Diagn.*, 2024, **3**, 1476–1493.
64 A. N. Acharya and A. Sahoo, *J. Mater. Sci.*, 2023, **58**, 12976–12992.
65 V. Salve, P. Agale, S. Balgude, S. Mardikar, S. Dhotre and P. More, *RSC Adv.*, 2025, **15**, 15651–15669.
66 P. Agale, V. Salve, S. Arade, S. Balgude and P. More, *Solid State Sci.*, 2025, **166**, 107960.
67 P. Agale, V. Salve, S. Mardikar, S. Patange and P. More, *Appl. Surf. Sci.*, 2024, **672**, 160795.
68 D. Balram, K.-Y. Lian and N. Sebastian, *Ultrason. Sonochem.*, 2020, **60**, 104798.
69 A. Biswal, P. K. Panda, A. N. Acharya, S. Mohapatra, N. Swain, B. C. Tripathy, Z.-T. Jiang and M. Minakshi Sundaram, *ACS Omega*, 2020, **5**, 3405–3417.
70 S. Mohapatra, H. T. Das, B. C. Tripathy and N. Das, *Adv. Sustainable Syst.*, 2024, **8**, 2400405.
71 J. C. Russell, V. A. Posey, J. Gray, R. May, D. A. Reed, H. Zhang, L. E. Marbella, M. L. Steigerwald, Y. Yang, X. Roy, C. Nuckolls and S. R. Peurifoy, *Nat. Mater.*, 2021, **20**, 1136–1141.
72 V. Augustyn, J. Come, M. A. Lowe, J. W. Kim, P.-L. Taberna, S. H. Tolbert, H. D. Abruña, P. Simon and B. Dunn, *Nat. Mater.*, 2013, **12**, 518–522.
73 I. Konuma, D. Goonetilleke, N. Sharma, T. Miyuki, S. Hiroi, K. Ohara, Y. Yamakawa, Y. Morino, H. B. Rajendra, T. Ishigaki and N. Yabuuchi, *Nat. Mater.*, 2023, **22**, 225–234.
74 T. Brezesinski, J. Wang, S. H. Tolbert and B. Dunn, *Nat. Mater.*, 2010, **9**, 146–151.
75 P. Simon and Y. Gogotsi, *Nat. Mater.*, 2008, **7**, 845–854.
76 B.-T. Liu, X.-M. Shi, X.-Y. Lang, L. Gu, Z. Wen, M. Zhao and Q. Jiang, *Nat. Commun.*, 2018, **9**, 1375.

77 K. Surya and M. S. Michael, *J. Mater. Sci.:Mater. Electron.*, 2022, **33**, 3139–3150.
78 R. Singhal, D. Thorne, M. Chaudhary, A. Kumar, S. Bhardwaj, R. Abazi, A. Colon, R. K. Gupta, J. Scanley, C. C. Broadbridge, B. P. Singh, P. K. LeMaire and R. K. Sharma, *AIP Adv.*, 2023, **13**, 1–8.
79 S. P. Patil and S. A. Jagadale, in *Spinel Ferrite Nanostructures for Energy Storage Devices*, Elsevier, 2020, pp. 123–145.
80 S. Swain, M. C. Tripathy, A. Sahoo, A. N. Acharya and S. Behera, *AEU-Int. J. Electron. Commun.*, 2024, **175**, 155114.